Tanguy Mertens

A new mapped infinite partition of unity method for convected acoustical radiation in infinite domains.

January 20, 2009

Université Libre de Bruxelles

Remerciements

Si tu donnes un poisson à un homme, il ne mangera qu'un jour. S'il apprend à pêcher, il mangera toute sa vie.

Proverbe de Confucius, repris plus tard par Dominique Pire dans le cadre de l'action Iles de Paix.

Je remercie Philippe Bouillard de m'avoir donné ma canne à pêche et conduit à l'étang. Je remercie Laurent Hazard et Guy Paulus pour tous leurs conseils avisés. Et tous les autres, famille, amis, qui ont gardé confiance en moi et m'ont encouragé à la persévérance.

C'est grâce à vous tous que je peux vous présenter avec fierté mon premier poisson.

Ceci dit, je voudrais remercier de manière plus académique tous les acteurs du projet.

Je remercie Philippe Bouillard qui est à la source du projet et qui a contribué à mon épanouissement scientifique durant cette aventure au sein du service BATir. Je remercie également pour leur encadrement: Guy Warzée pour sa gentillesse et sa patience ainsi que Jean-Louis Migeot pour son soutien industriel et ses remarques pertinentes.

Ce passage au service BATir a été une expérience riche sur le plan scientifique mais aussi humain. Je remercie mes collègues de l'ULB pour les relations que nous avons construites ensemble, pour les activités dans le cadre du travail ou hors des murs de l'université. Je pense évidemment à Laurent Hazard et à Guy Paulus, pour leur amitié mais aussi leur disponibilité et leurs nombreux conseils. Merci aussi à tous les membres du service des milieux continus qui ont ajouté une dimension humaine. La nature des contrats de recherche et d'assistanat est tel qu'ils furent nombreux a être passés par les murs de l'université. Je ne pourrai tous les citer mais je tiens quand même à remercier personellement Katy, Erik, Geneviève, Yannick, Louise, Dominique, Thierry, Sandrine, Bertha, David, Benoît, Peter et Kfir.

S'il est vrai qu'un travail de thèse tend à rendre le chercheur autonome, les collaborations et interactions restent importantes. Je remercie à cet égard toute l'équipe de l'Institute of Sound and Vibration Research de l'université de Southampton. Je remercie Jeremy Astley, chef du service de m'y avoir accueilli pendant un stage de six mois. Je le remercie aussi pour l'environnement de travail de qualité qu'il m'a offert. Il est évident que la présence de Pablo Gamallo à l'I.S.V.R. a énormément contribué à l'aboutissement de ce travail de recherche. Je le remercie pour tout le temps qu'il m'a consacré, à Southampton et même par la suite lors de contacts e-mail ou lors de rencontres en conférences. Je le remercie pour l'intérêt qu'il porte à la présente étude, pour ses encouragements et pour tous ses enseignements. Mais ce séjour n'a pas été que professionellement enrichissant, je repense à l'accueil qui m'a été réservé ainsi que de nombreux excellents souvenirs qui font de ce séjour une partie inoubliable de ma vie. Je tiens donc à remercier chaleureusement pour leur amitié précieuse Vincent et Theresa, Luigi, Claire, Naoki, Rie, Sue, Lisa, Eugene, Isa, Daniel et Stéphanie, Alessandro et Emmet.

Ces quelques lignes indiquent à quel point les relations humaines ont une influence sur ma vie. Cela ne sera pas une surprise alors si je remercie les personnes pour qui je *travaille dans les avions* ou ceux qui me félicitent de mon travail, *les semaines durant lesquelles, ils n'ont pas trop entendu les avions*. Je pense bien entendu à ma famille, principalement ma maman, pour avoir fait de moi l'homme que je suis aujourd'hui et mes amis, plus particulièrement mes collocataires: Iyad, Mathieu, Quentin, Guerrick, Caroline et Florence. Merci à vous de partager mes valeurs et de colorier mon existence.

Enfin, je terminerai par remercier les deux petits rayons de soleil qui ont ensoleillé la fin de ce long parcours.

List of Symbols

Greek symbols

β	: $\sqrt{1-M_0^2}$	
γ	: Poisson ratio of specific heat capacities : c_p/c_v	
Γ	: interface separating the inner and the outer domains	
ε	: Error	
μ	: phase function	$[m]$
ρ	: mass density	$[kgm^{-3}]$
ρ_0	: steady mean density	$[kgm^{-3}]$
ρ_a	: acoustic density	$[kgm^{-3}]$
$\boldsymbol{\sigma}$	: stress tensor	$[Nm^{-2}]$
ϕ	: velocity potential	$[m^2s^{-1}]$
ϕ_0	: mean velocity potential	$[m^2s^{-1}]$
ϕ_a	: acoustic velocity potential	$[m^2s^{-1}]$
$\tilde{\phi}_a$	: amplitude of the harmonic acoustic velocity potential	$[m^2s^{-1}]$
$\tilde{\phi}^h$	: numerical approximation of $\tilde{\phi}_a$	$[m^2s^{-1}]$
$\tilde{\phi}_h^I$	: numerical approximation in the outer region Ω_o	$[m^2s^{-1}]$
Φ_α	: shape function for the α^{th} degree of freedom	
Φ_α^I	: infinite shape function for the α^{th} degree of freedom	
ω	: angular frequency	$[s^{-1}]$
Ω	: domain	
Ω_i	: inner region	
Ω_o	: outer region	

Arabic symbols

$\tilde{a}_n$	: normal acceleration of a vibrating wall	$[ms^{-2}]$
A_n	: normal acoustic admittance	$[m^2skg^{-1}]$
$A^{\pm}_{mn}$	: incident and reflected modal amplitude	$[m^2s^{-1}]$
c	: speed of sound	$[ms^{-1}]$
c_0	: steady mean part of the speed of sound	$[ms^{-1}]$
c_∞	: speed of sound at large distance from the source	$[ms^{-1}]$
c_p	: specific heat capacity at constant pressure	$[JK^{-1}]$
c_v	: specific heat capacity at constant volume	$[JK^{-1}]$
$dofs$	: number of unknowns of the approximation	
E	: energy flow out of a surface	$[J]$
$E^{\pm}_{mn}$	: incident and reflected modal patern	
f	: excitation frequency	$[s^{-1}]$
G	: geometric factor	
h	: mesh size	$[m]$
H	: Hilbert space	
i	: imaginary unit $= \sqrt{-1}$	
$\mathbf{I}$	: Sound intensity	$[Wm^{-2}]$
J'	: stagnation entropy	$[Jkg^{-1}]$
k	: wavenumber	$[m^{-1}]$
$k^{\pm}_{r,mn}$	: incident and reflected radial wavenumber	$[m^{-1}]$
k_B	: Boltzmann constant	$[JK^{-1}]$
$K^{\pm}_{z,mn}$	: incident and reflected axial wavenumber	$[m^{-1}]$
L^d_j	: Legendre polynomial of order d for node j	
L_s	: curve enclosing the boundary S_s	
L_v	: curve enclosing the boundary S_v	
m	: angular mode number	
$\mathbf{m}'$	: mass flux	$[kgm^-2s^{-1}]$
m_0	: radial order of the infinite element	
m_w	: mass of a molecule	$[kg]$
M_0	: mach number	
M_i	: Mapping function for node/point i	
$\mathbf{n}$	: outer normal to the domain	
n	: radial mode number	
n^I_d	: number of infinite degree of freedom	
$n\,(j)$	: size of the local approximation space at node j	
nni	: number of infinite nodes	
$nodes$	: number of nodes	
N_i	: Partition of Unity function of node i	
N_m	: number of angular modes	
N_n	: number of radial modes	
N_M	: number of reflected modes (unknown)	

p	: fluid pressure	$[Pa]$
p_0	: steady mean fluid pressure	$[Pa]$
p_a	: acoustic pressure	$[Pa]$
$\tilde{p}_a$	: amplitude of the harmonic acoustic pressure	$[Pa]$
$\tilde{p}_{an}$	: analytic amplitude of the harmonic acoustic pressure	$[Pa]$
$\mathbf{q}$	: heat flux	$[Wm^{-2}]$
Q_w	: heat production	$[J]$
r_o	: distance to the source point	$[m]$
R	: specific gas constant	$[JK^{-1}mol^{-1}]$
R_j	: radial function for infinite node j	
R_j^d	: radial function of order d for node j	
s	: entropy	$[Jkg^{-1}K^{-1}]$
S	: boundary	
S_i	: mapping functions for the interface $\mathit{\Gamma}$	
S_M	: Modal boundary	
S_s	: soft wall	
S_v	: vibrating wall	
t	: time	$[s]$
T	: Temperature	$[K]$
T_j	: circumferential function for infinite node j	
$\tilde{u}_n$	: normal displacement of a vibrating wall	$[m]$
$\mathbf{v}$	: fluid velocity	$[ms^{-1}]$
$\mathbf{v}_0$	: steady mean fluid velocity	$[ms^{-1}]$
$\mathbf{v}_\infty$	: fluid velocity at large distance from the source	$[ms^{-1}]$
$\mathbf{v}_a$	: acoustic velocity	$[ms^{-1}]$
$\tilde{\mathbf{v}}_a$	: amplitude of the harmonic acoustic velocity	$[ms^{-1}]$
$\mathscr{V}$	: the Sobolev space $W^{1,2} = H^1 = \{f : f, \nabla f \in L^2\}$	
V_{jl}	: l^{th} local approximation function of node j	
$\tilde{w}_n$	: normal velocity of a vibrating wall	$[ms^{-1}]$
W_j	: weight function of node j	
W_j^I	: infinite weight function of the infinite node j	
$W_{M,nm}$	: modal weight function of the angular and radial mode (m, n)	

Operators

∇	: gradient operator
$\nabla\cdot$	: divergence operator
$\nabla\times$	: curl operator
$\mathit{\Delta}$	: Laplacian operator
$\frac{D}{Dt}$	: Total time derivative
$:$	: the double dot product of two tensors
$\langle\ \rangle$	: time average
$\Re$	: Real part

Contents

5

Axisymmetric formulation: performance analysis

This chapter analyses the performances of the axisymmetric Mapped Infinite Partition of Unity formulation. We consider applications such as duct propagation, multipole radiation or rigid piston radiation to illustrate the accuracy and the efficiency of the method. To assess the performances, we plot two types of curves: convergence and performance. The convergence curve plots the L^2 relative error with respect to the number of degrees of freedom. This gives an indication of the accuracy of the method and the enrichment functions with respect to the number of unknowns. However, it does not give any information on the time required to compute the matrices (numerical integration), the bandwidth of the matrices nor the time required to solve the system. The efficiency of the method is then evaluated by comparing the time required to compute a solution which is under a certain level of accuracy. This is the performance curve.

The L^2 relative error is obtained by expression:

$$\varepsilon_r = \frac{\sqrt{2\pi \int_{\Omega_i} r\,(\tilde{p}_{an} - \tilde{p}^h)\,(\tilde{p}^*_{an} - \tilde{p}^{h*})d\Omega}}{\sqrt{2\pi \int_{\Omega_i} r\,(\tilde{p}_{an})\,(\tilde{p}^*_{an})d\Omega}} \tag{5.1}$$

where $\tilde{p}_{an}$ and $\tilde{p}^h$ are the exact and computed pressure, respectively and $\tilde{p}^{h*}$ denotes the complex conjugate of $\tilde{p}^h$. This integration is performed following the Gauss Legendre integration scheme.

The computations are performed on a HP XC cluster Platform 4000 composed of 32 nodes. Each node is a HP Proliant DL 585 containing four CPUs AMD Opteron Dual Core at 2GHz. We have been allowed to use a queue intended for 8 processor and 32GB of RAM per job. The Mapped Infinite Partition of Unity Method is implemented in Matlab. The linear system of equations is solved using UMFPACK 5.0.2 [45, 46, 47, 48, 49], a set of routines solving sparse linear systems via LU factorization.

5.1 Duct propagation

This section illustrates the performances of the Mapped Infinite Partition of Unity Method. Computed results are compared to analytical solutions. The method is also compared to the Finite Element Method: ACTRAN^{TM} linear and quadratic elements. Results of the linear Finite Element Method may also be obtained with the '*degenerated*' Partition of Unity Method.

We also focus on other considerations such as the use of a variable enrichment (i.e. not the same enrichment on all the nodes of the mesh) and the evaluation of the condition number and its effect on the solution.

5.1.1 Convergence and performance analyses

Convergence and performance curves analyse the method by means of L^2 relative error (5.1).

The convergence curve plots at a given excitation frequency, the L^2 relative error of the numerical solution with respect to the number of degrees of freedom. The number of degrees of freedom gives an idea of the size of the matrices but it does not give any information on the number of non-zero terms in the matrix, its bandwidth or the condition number. Yet, all these parameters will influence the global computational effort. The performance curve plots the time required by the algorithms to achieve the resolution under a certain level of error. This is done for several non-dimensional wavenumbers (ka). This allows us to compare the global performance, the real effort of the computation. Nevertheless, it is difficult to compare methods coded in different languages.

We consider acoustic propagation in a hard walled infinite cylindrical duct of radius $R_d = 0.5m$ and then a diameter $D = 1m$. The computational domain corresponds to a part of the duct which is $L = 2m$ long[1]. Modal and transmitted boundary conditions simulate semi-infinite ducts at both ends of the computational domain (fig. 2.18).

The analytical solution for the pressure ($\tilde{p}_{an}$) in a duct is given by the following modal decomposition [44]:

$$\tilde{p}_{an}(r, z, \theta) = \sum_{m=-\infty}^{\infty} \sum_{n=1}^{\infty} J_m(k_{rmn} r)\, e^{im\theta} \left(a_{mn}^{+} e^{-ik_{zmn}^{+} z} + a_{mn}^{-} e^{+ik_{zmn}^{-} z} \right) \tag{5.2}$$

where J_m is the Bessel function of order m. The radial k_{rmn} and longitudinal $k_{zmn}^{\pm}$ wavenumbers are obtained by resolving equations (5.3).

[1] This is a difference with previous results in the verification section which were obtained for a duct length of $L = 1m$. The length of $1m$ has been chosen to corresponds to the three-dimensional application such that figures can be compared, while this analysis has been performed for paper [69].

$$\begin{aligned} J_m' \left(k_{rmn} R_d\right) &= 0 \\ k_{zmn}^{\pm} &= \frac{\mp k M_0 + \sqrt{k^2 + \left(1 - M_0^2\right) k_{rmn}^2}}{\left(1 - M_0^2\right)} \end{aligned} \tag{5.3}$$

The performance of the convected Mapped Infinite Partition of Unity Method is compared to the Finite Element Method (linear and quadratic elements). In this case we restricted the analysis by simulating the propagation of the second mode ($n = 2$) of the first azimuthal order ($m = 1$). This is simulated by prescribing modal boundary conditions (section 2.9.2 with $E_n^{\pm} = J_m\left(k_{r,n} r\right)$) at both ends of the duct. The modal boundary condition at the inlet ($x = 0\ m$) prescribes the second mode of the first azimuthal order traveling in the duct direction $\left(n = 2,\ m = 1,\ A_2^{+} = 1\right)$, and allows the boundary to be permeable to the propagation of all cut-on modes coming from the computational region: all $\left(A_n^{-}\right)$ such that $k_{z,n}^{-}$ is real, are unknowns. At the outlet ($x = 2\ m$), we allow the boundary to be permeable to all cut-on modes going outside the domain. Modes coming from the right end of the duct are set equal to zero to create an anechoic termination.

Figure 5.1 illustrates the distribution of the real part of the pressure in the duct. Note that this figure corresponds to an axisymmetric cut in the duct (domain Ω). The pressure in the whole duct can be obtained by rotating the presented results around the x axis with a scaling factor of $e^{-im\theta}$, for this application, $m = 1$. The excitation frequency is chosen equal to 800 Hz ($kD = 14.78$). This application has been analysed in the previous sections for the '*no-flow*' and the convected cases. The convected wave propagation considers a uniform mean flow ($\mathbf{v} = -100 m/s \mathbf{1}_z$) moving in the opposite direction of the wave.

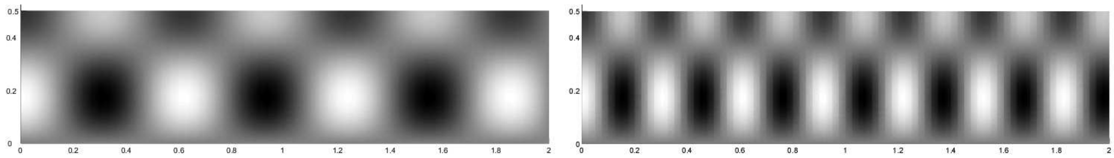

(a) (b)

Fig. 5.1. Real part of the pressure of the second mode $n = 2$; azimuthal order $m = 1$, excitation frequency: 800Hz ($kD = 14.78$) (a) No flow (b) Uniform mean flow with a mach number of ($\mathbf{M} = -0.297\mathbf{1}_z$).

A convergence analysis is performed to illustrate and compare asymptotic convergence rates on this duct application at 800 and 2000 Hz with a non-dimensional wavenumber $kD = 14.78$ and $kD = 36.96$ respectively. The congergence curves for a frequency of 800 Hz are given in figure 5.2 and in figure 5.3 for 2000 Hz. The convergence curve gives the relative error in percent with respect to the number of degrees of freedom (dofs). The number of degrees of freedom corresponds to the size of the matrix system. It is equal to the number of nodes and the number of modal unknowns for Finite Element Method. For the Partition of Unity Method, it is the number of nodes times the degrees of freedom per node and the number of modal unknowns. The convergence compares the Finite Element Method (linear and quadratic elements) with the Partition of Unity Method. Several polynomial enrichments are used. The order of these polynomial terms varies from 0 to 6 generating complete and incomplete polynomial functions up to order six. All the meshes have been generated by taking a number of elements along the z direction as being 3 times larger than the number of elements in the r direction.

As expected, figure 5.2(a) shows that linear Finite Elements are equivalent to the Partition of Unity Method with a constant enrichment: $V_{j1} = \{1\}$. The same remark stands for quadratic Finite Elements compared to the first order enrichment. This can be explained considering that the shape function is the product of the partition of unity function, which is linear, and the enrichment (linear in this case). It leads to quadratic shape functions. It is then easily understandable why simulations with a first order enrichment corresponds to the quadratic FEM.

As predicted, the convergence rate of the Partition of Unity Method with a complete quadratic enrichment is better than for the linear and the quadratic Finite Element Method. A quadratic enrichment corresponds to the use of a cubic polynomial for the approximation. The convergence rate of the method depends on the polynomial order chosen for the enrichment (as illustrated in figures 5.2(a) and 5.3(a)). Note that high polynomial functions lead to instabilities but it occurs for very low level of errors.

Figures 5.2(b) and 5.3(b) illustrate the effect of non complete polynomial sets at two different frequencies until order 3. Complete sets of polynomials always have the best rates of convergence. Some non complete bases also exhibit the same rate. These 'performant' non complete sets are those which does not have the cross terms. This is probably due to the existence of the cross terms thanks to the product of partition of unity functions by the enrichment terms. We also remark that the terms z and r should not be removed because then the convergence does not behave like a p order approximation anymore.

A family of fourth order sets is presented in figures 5.2(c) and 5.3(c). The same conclusions can be drawn. Some incomplete basis have the same convergence rate than the full set (in general when some cross terms are removed) but there is a drop in accuracy when x^n $(n < p)$ terms are removed. Note that instabilities appears for low level of error.

The performance curve is shown in figure 5.4. These curves correspond to the time required to compute a solution under a level of relative error ($\varepsilon_r < 5\%$). This is done along a frequency range varying from 800 Hz ($kD = 14.78$) to 7000 Hz ($kD = 129.36$). Meshes have been generated with 3 times more elements in the axial z direction than in the radial r one. Figure 5.5 shows the coarsest mesh used for the simulation using the second order enrichment at 800 Hz.

The advantage of this performance curve is that the CPU time takes into account the whole process and so the real effort required for the computation. The drawback is the difficulty to compare methods which have been implemented in different languages such as C or MATLAB. This is the reason why only Partition of Unity curves are presented. These

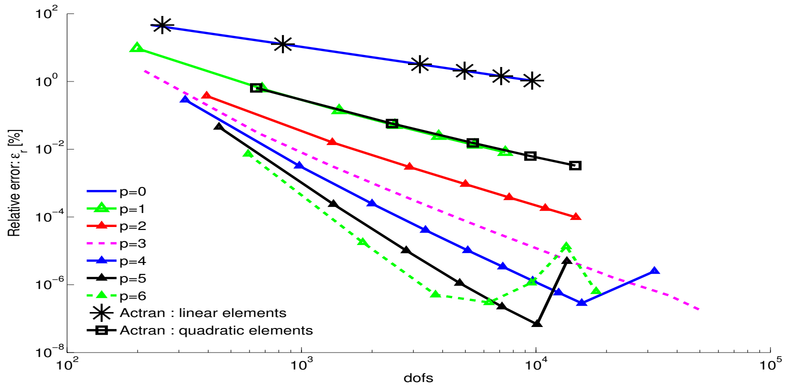

(a)

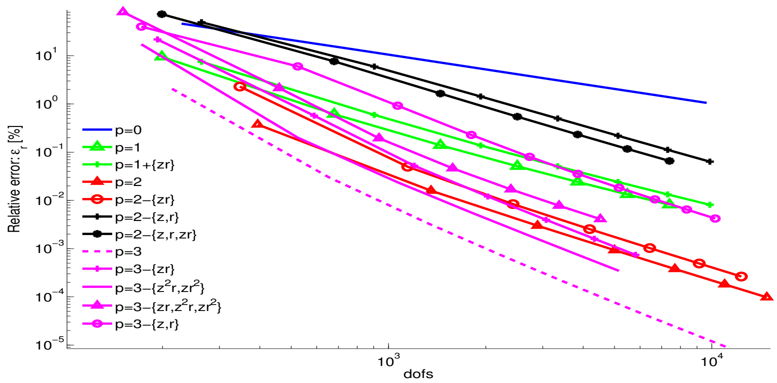

(b)

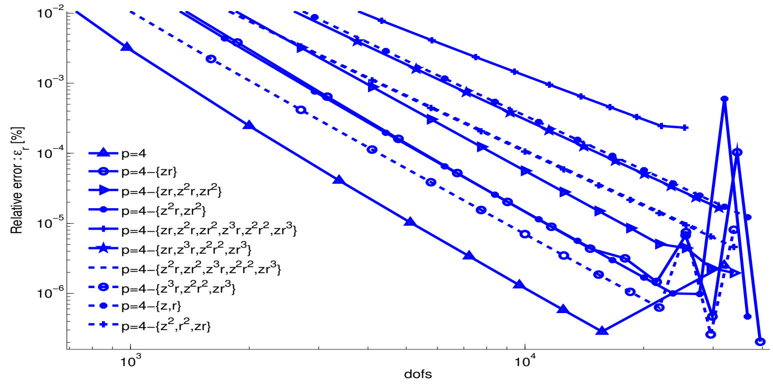

(c)

Fig. 5.2. Relative error (ε_r [%]) plotted with respect to the number of degrees of freedom (dofs): propagation of the second mode ($n = 2$), first axisymetric order ($m = 1$) and excitation frequency 800 Hz ($kD = 14.78$). Enrichment functions: Complete set of polynomial functions of order p up to order 6 (a) - Complete and incomplete sets up to order 4 (b) - complete and incomplete sets for the fourth order (c).

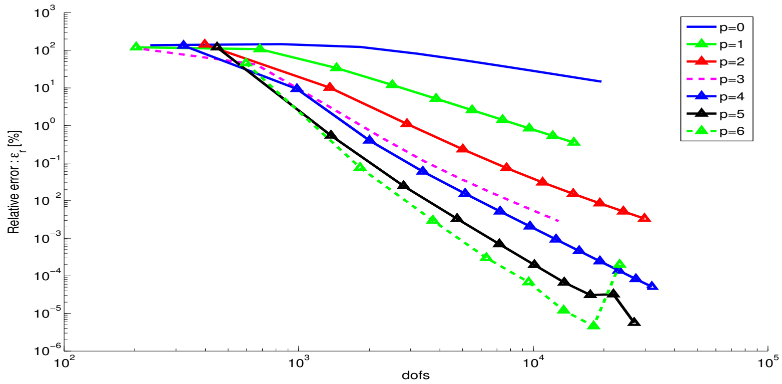

(a)

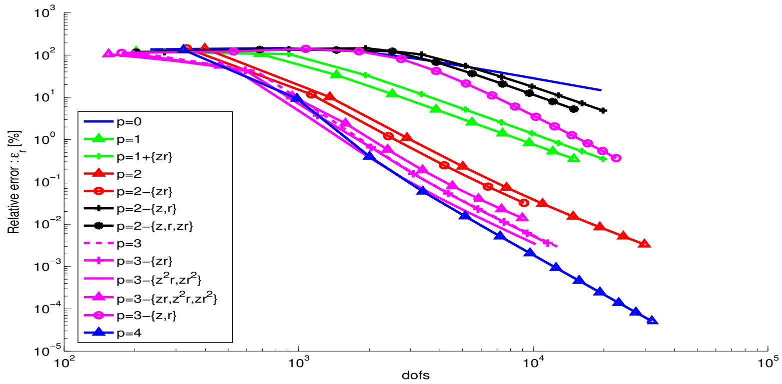

(b)

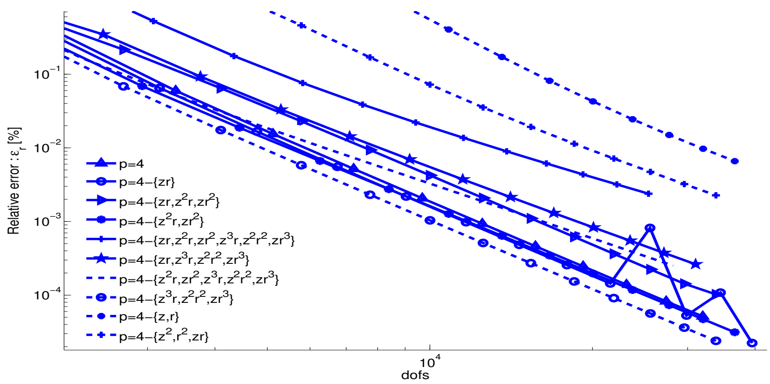

(c)

Fig. 5.3. Relative error (ε_r [%]) plotted with respect to the number of degrees of freedom (dofs): propagation of the second mode ($n = 2$), first axisymetric order ($m = 1$) and excitation frequency 2000 Hz ($kD = 36.96$). Enrichment functions: Complete set of polynomial functions of order p up to order 6 (a) - Complete and incomplete sets up to order 4 (b) - complete and incomplete sets for the fourth order (c).

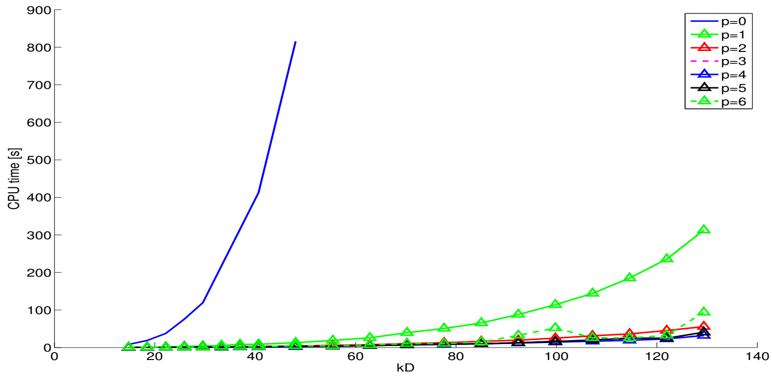

(a)

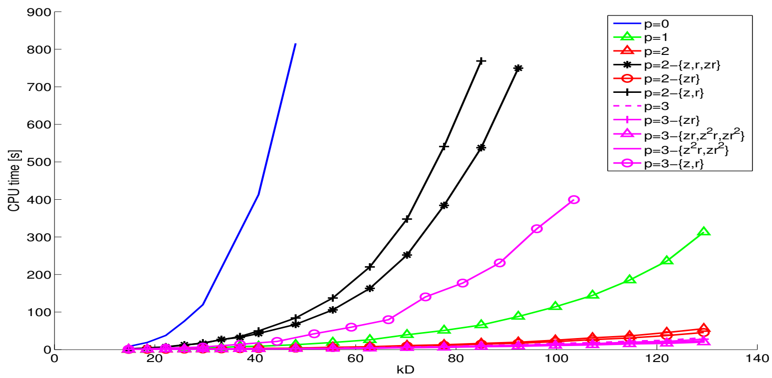

(b)

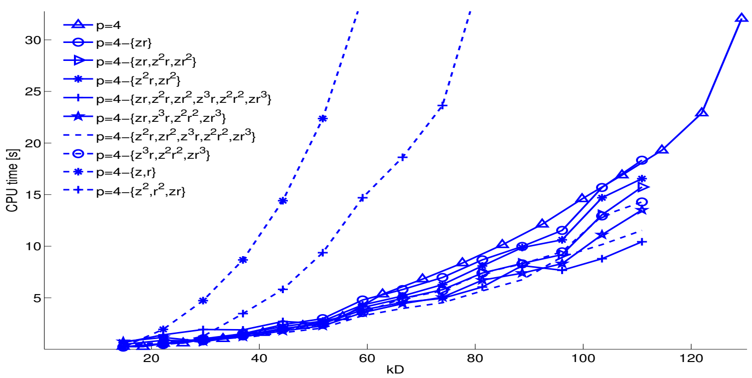

(c)

Fig. 5.4. Computational Time (s) versus the non-dimensional wavenumber (kD) with an accuracy under 5%, frequency varying from 800Hz to 7000Hz, the characteristic length D is the diameter of the duct. Enrichment functions: Complete set of polynomial functions of order p up to order 6 (a) - Complete and incomplete sets up to order 4 (b) - complete and incomplete sets for the fourth order (c).

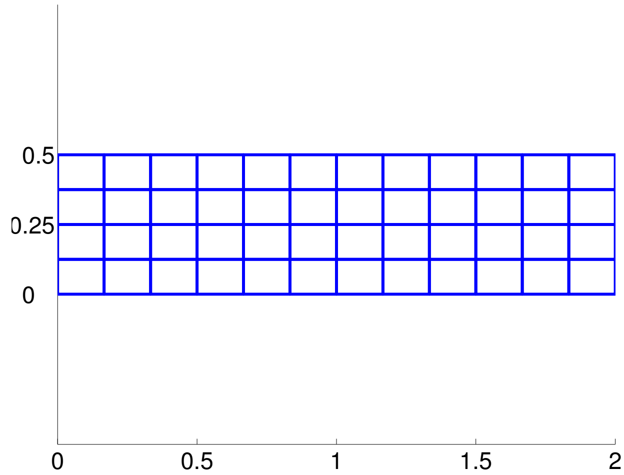

Fig. 5.5. Coarsest mesh of the duct used for the simulation of the propagation at 800Hz with the second order enrichment .

results show the efficiency of the proposed method. A high polynomial order enrichment requires less computation time to solve the application within an accuracy of 5% at a given frequency. To solve the application with a kD equal to 31, the linear elements requires 263 seconds while the non-complete second order enrichment (without the cross term zr) only requires 1.93 seconds. The gain is a speed up of a factor 136. From another point of view, at the same CPU time, the high order enrichment allows to reach higher frequencies. For instance, a CPU time of 35 seconds allows to solve the application with a kD equal to 20 for linear elements and a kD equal to 90 for the second order enrichment without zr. The proposed method with the incomplete second order enrichment reaches frequencies five times higher than the classical linear Finite Element Method within the same amount of time. This is exactly the expected performance. While the polynomial order increases, we expect the required amount of time to decrease. However, at high frequencies $ka > 130$ (figure 5.6), higher orders than 4 look to be less performant. This is due to a problem of instability as it is also observed for the convergence analysis. Non-complete basis (without z^n or r^n terms with $n < p$) are not efficient, as it has been observed during the convergence analysis. However non-complete bases without cross terms behave like the complete one. We can see in figure 5.4(c) that some non-complete fourth order bases are more performant than the full fourth order. Due to instabilities at high order enrichment, we recommend the use of polynomial enrichment up to order 4.

The Partition of Unity Method with a polynomial enrichment of order s behaves like a p-FEM of polynomial order $s + 1$. The advantage of such a method compared to the p-FEM one is the possibility to refine locally the solution without refining the mesh. In many ducted problems for example one has '*hot spots*' where the Mach number is high in a small region and one must normally refine the mesh. This method would allow to enrich the nodes of this region with higher polynomial functions.

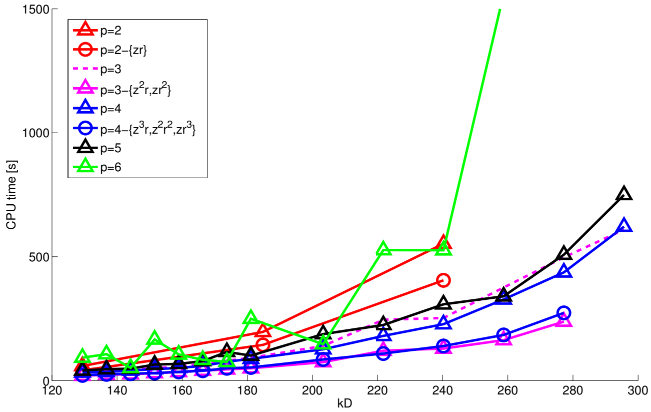

Fig. 5.6. Computational Time (s) versus the non-dimensional wavenumber (kD) with an accuracy under 5%, frequency varying from 7000Hz to 16000Hz, the characteristic length D is the diameter of the duct. Enrichment functions: Complete and incomplete sets of polynomial functions of order p up to order 6 .

5.1.2 Local enrichment

We will now discuss the effect of enriching nodes locally. The idea is to show that we can easily enrich some nodes of the mesh. This is then illustrated on two applications[2]. We first analyse the effect of local enrichment on the propagation of an evanescent wave in a cylindrical duct. We then analyse the case of the non-uniform duct with uniform mean flow.

The first application considered is a hard walled cylindrical duct ($L = 1m, R_d = 0.5m$). We analyse the propagation of an evanescent mode at 800 Hz in the duct ($m = 1, n = 4$). As it is an evanescent mode, we expect the pressure to decay exponentially (fig. 3.7). We are interested in the accuracy of the solution in the whole domain, we hence compare the L^2 relative error of four different configurations on two different meshes (8 cases). The first mesh is composed of 30 axial elements and 10 in the radial one. The second mesh contains 50 elements in the axial direction and 20 in the radial one. The four configurations correspond to the way nodes have been enriched:

- all nodes with the constant enrichment: $V_{j1} = \{1\}$.
- the first 5 columns of nodes enriched with a second order subspace:
$$V_{jl} = \left\{1, (z - z_0), (r - r_0), (z - z_0)^2, (r - r_0)^2\right\},$$
the other nodes with the constant enrichment $V_{j1} = \{1\}$.

[2] A third application has been anlaysed but it does not correspond to acoustic propagation in ducts. Please refer to appendix 10.5

- the first 10 columns of nodes enriched with a second order subspace:

$$V_{jl} = \left\{1, (z - z_0), (r - r_0), (z - z_0)^2, (r - r_0)^2\right\},$$

  the other nodes with the constant enrichment $V_{j1} = \{1\}$.

- all nodes with the second order enrichment:

$$V_{jl} = \left\{1, (z - z_0), (r - r_0), (z - z_0)^2, (r - r_0)^2\right\}.$$

Table 5.1 gives the L^2 relative error and the number of degrees of freedom obtained for the two meshes with the four different enrichments: No column of nodes enriched, 5 columns of nodes enriched, 10 columns of nodes enriched and all nodes enriched.

Relative error Degrees of freedom	No column	5 columns	10 columns	all columns
30 X 10	9.2755%	0.6162%	0.0887%	0.0835%
	341 dofs	561 dofs	781 dofs	1705 dofs
50 X 20	2.33%	0.4853%	0.0796%	0.0065%
	1071 dofs	1491 dofs	1911 dofs	5355 dofs

Table 5.1. Evaluation of the effect of local enrichment on the L^2 relative error for the propagation of an evanescent mode ($800Hz, m = 1, n = 4$) in a hard walled cylindrical duct ($L = 1m, R_d = 0.5m$)

By looking at the table we may first conclude that the more refined mesh and the more enriched nodes, the best accuracy.

However, we are also looking for performance. This means we care about the accuracy but also the number of unknowns. These applications show that enriching a few nodes close to the modal boundary condition is more convenient and accurate that remeshing the whole domain (e.g.: 0.6162% for 561 dofs compared to $2.33\%, 1071dofs$).

We then conclude that local enrichment is very efficient when the pressure shows complex distribution on local area. It allows to increase the accuracy of the global solution without refining the mesh.

Note that these results do not only stand for evanescent modes. What has to be understood is that enriching nodes close to complex pressure distribution is beneficial for the performance (significant increase of accuracy without remeshing and providing low additional unknowns). This conclusion is also valid whatever the application as soon as we can isolate the region to enrich: high Mach number, edges, evanescent modes.

The second illustration corresponds to the convected propagation of a plane wave at 800Hz (ka=14.8 for a=1m) in a non-uniform duct (same geometry as in section 3.2). We obtained a reference solution with a Finite Element computation on a fine mesh: 101101 nodes. The flow (figure 3.15) has been computed on this fine mesh, it has then been used for other computations (coarser meshes). We generated two other meshes: mesh1 with 4221 nodes and mesh2 with 20541 nodes and computed the acoustic potential for 4 configurations. The first one consists in enriching all the nodes with the constant enrichment (p=0). We then enriched region A (figure 5.7) with polynomial functions of order 2 (p=2). The third configuration correspond to enriching both regions A and B. And finally, we consider the case with all nodes with an enrichment of order 2 (p=2).

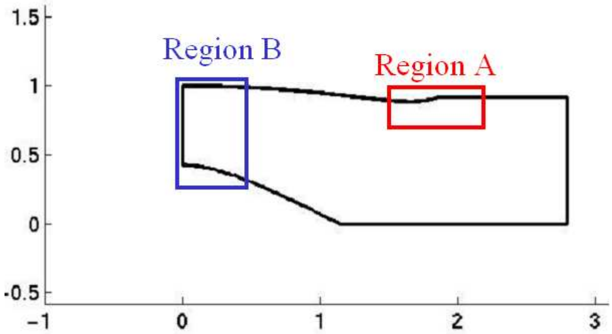

Fig. 5.7. Illustration of the geometry of the application and the regions to be enriched.

Table 5.2 illustrates that the enrichment of local areas improves the accuracy of the solution. It is then not necessary to generate a new mesh, finer at special regions. The approximation may be improved by locally increasing the order of the enrichment functions. Of course, it is obvious that enriching all the nodes or generating a finer mesh for the whole application will give more accurate results than only modifying the enrichement functions at some nodes. But then you have to deal with a larger computational system.

Relative error Degrees of freedom	only p=0	Region A	Regions A and B	only p=2
mesh1 4221 nodes	29.92%	26.05%	19.22%	5.65%
	4240 dofs	5490 dofs	9270 dofs	25345 dofs
mesh2 20541 nodes	5.31%	4.9%	3.9621%	
	20560 dofs	26525 dofs	44975 dofs	

Table 5.2. Evaluation of the effect of local enrichment on the L^2 relative error for the convected propagation of a plane wave in a non-uniform duct ($800Hz, m = 0, n = 1$). Note that the values for the case p=2 for all the nodes of mesh2 are not indicated as it corresponds to more degrees of freedom than the reference solution.

5.1.3 Conditioning

Conditioning is an important topic in computational methods such as the Partition of Unity Method (polynomial or trigonometric enrichments [17, 18]), the Discontinuous Galerkin Method [70], the Ultra Weak Variational Formulation [16, 19], etc.

In the case of plane wave bases, the condition number increases with the number of nodes in the mesh. Note that this increases even quicker with a high number of plane waves in the enrichment. One way of reducing this condition number is, for instance, to use a non-uniform number of plane waves per nodes [19], another one is the use of an appropriate preconditioner. This increase in condition number is due to linear dependencies, very different sets of amplitude can represent the same acoustic field within an element [17]. The risk is a loss of accuracy, but the authors cited in this section showed that the solution remains accurate. They showed curves illustrating that the increase in the condition number does not prevent the error to decrease. Gamallo et al. [16] showed that as long as the solution is smooth, they obtain good accuracy even for high condition numbers (e.g.: cond=10^{24}). Figure 5.8 (issued from [18]) illustrates the decay of the L^2 error with respect to the number of non-zero terms (nnz) populating the matrix and with respect to the condition number. This has been obtained for the Partition of Unity Finite Element Method (plane wave enrichment) and the Ultra Weak Variational Formulation for the propagation in a two-dimensional hard walled duct of height $h = 1m$ and length $l = 2m$. They prescribed the propagation of the 12^{th} mode for the non-dimensional wavenumber $kh = 40$. For more details, please refer to [18]. Figure 5.8 shows that the increase of the condition number, related to the increase of the number of non-zero terms, does not affect the decrease of the error. Low level of error can be reached without being disturbed by the conditioning.

However, Gamallo et al. [18, 16] showed that in the particular case of singular solutions (e.g.: wave propagation in a L-shaped domain) the increase in condition number could lead to a decrease in accuracy. This is illustrated in figure 5.9 (issued from [18]). The results correspond to wave propagation in a two-dimensional L-shaped domain for the wavenumber $ka = 40$ (for more details about the geometry, boundary conditions or the analytic solution, please refer to [18]). Figure 5.9 shows that the error starts increasing from a certain number of non-zero terms. This is unusual as we expect the error to decrease with mesh refinement. The ill-conditioning has a negative effect on the accuracy. This prevents the error to decrease below 1% in the coarse mesh. Note that the use of a non-uniform number of plane wave in the basis functions allows to improve the condition number and leads to better performances.

Aware of all these considerations, we evaluate the effect of the condition number on the accuracy of the simulation using the Partition of Unity Method with polynomial enrichment. Figures 5.10, 5.11 and 5.12 illustrate the relation which exists between the number of degrees of freedom, the condition number and the accuracy (represented by the L^2 relative error). These results correspond to the simulation of the propagation of the second radial

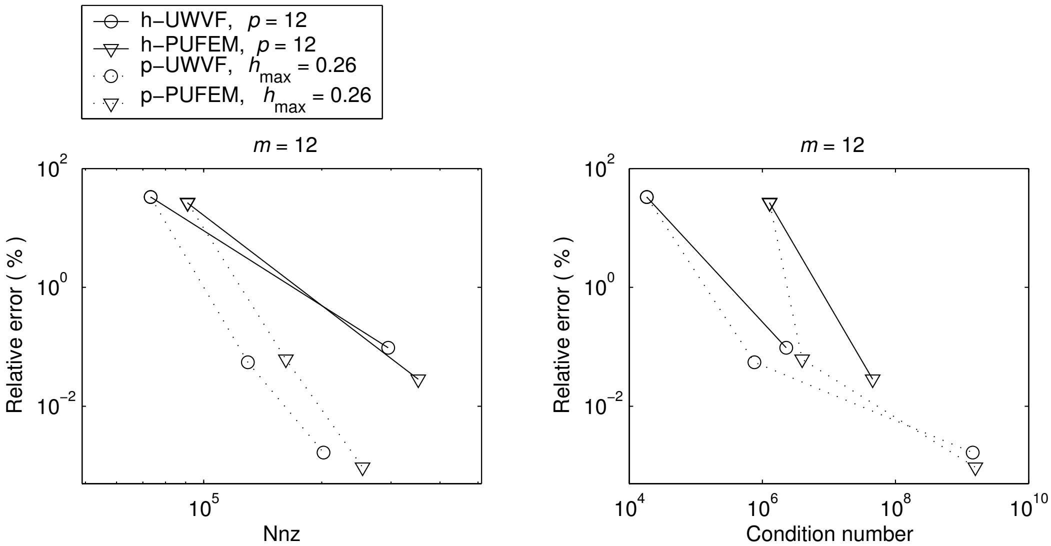

Fig. 5.8. Reproduced from [18]. A comparison of the two strategies for improving the accuracy. The errors presented using solid lines are computed by refining the mesh ($h_{max} = 0.26m$ & $h_{max} = 0.13m$) and using a fixed number of basis functions (12). Dotted line errors are computed in the coarser mesh ($h_{max} = 0.26m$) and by increasing the basis dimension. The results are shown for the non-dimensional wavenumber $kh = 40$ and for the 12^{th} mode.

mode $n = 2$ of the first azimuthal order $m = 1$ at 800 Hz in a hard walled duct. The duct is $2m$ long and its radius is $0.5m$.

As the mesh is refined, the number of degrees of freedom increases and the error decreases (fig. 5.10). The convergence rate depends on the enrichment used. Note that it is not a good idea, in terms of accuracy, not to include the linear terms $(z - z_0)$ and $(r - r_0)$ in the second order enrichment. Figure 5.11 illustrates the evolution of the condition number with respect to the number of degrees of freedom. The condition number is calculated with the MATLAB function *cond*. If the matrix is well conditioned, *cond* is close to 1. It increases for poorly condition systems. In the case of the enrichments $V_{j1} = \{1\}$ and $V_{jl} = \{1, (z - z_0)^2, (r - r_0)^2\}$, the condition number increases with the number of degrees of freedom. However, for other enrichments the condition number is directly around a high value: $cond = 10^{18}$. This means that the system is ill-conditioned even for coarse meshes. This can be explained with the linear dependencies which exist in the shape functions: $N_j V_{jl}$.

Hazard [71] also observed this ill-conditioning in the case of polynomial Partition of Unity Method applied to plate vibration. He observed a difference between the size of the matrix and its rank (number of linearly independent columns or rows). This illustrates the presence of linear dependencies. Aiming at reducing the condition number, he proposed to use shifted enrichment functions $\{z - z_0\}$ instead of $\{z\}$ and prevent nodes with prescribed essential boundary conditions to benefit from enrichment functions. However, he has not used these modifications since he dealt with the UMFPACK solver [45] which handles well bad conditioned matrices.

Figure 5.12 confirms that high condition numbers do not prevent to reach good accuracy levels. It can also be seen in figure 5.10 that the convergence rates are not affected by the increase of the number of degrees of freedom. Note that the same behavior is also obtained for higher polynomial orders. For instance, the condition number of the complete polynomial of order 6 has a condition number variyng between $1\ 10^{20}$ to $5\ 10^{20}$.

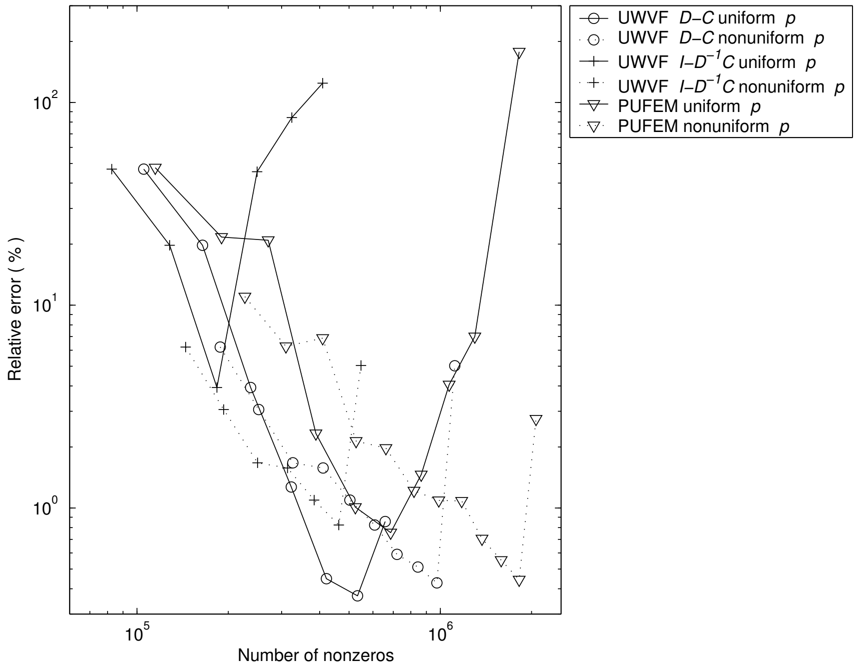

(a)

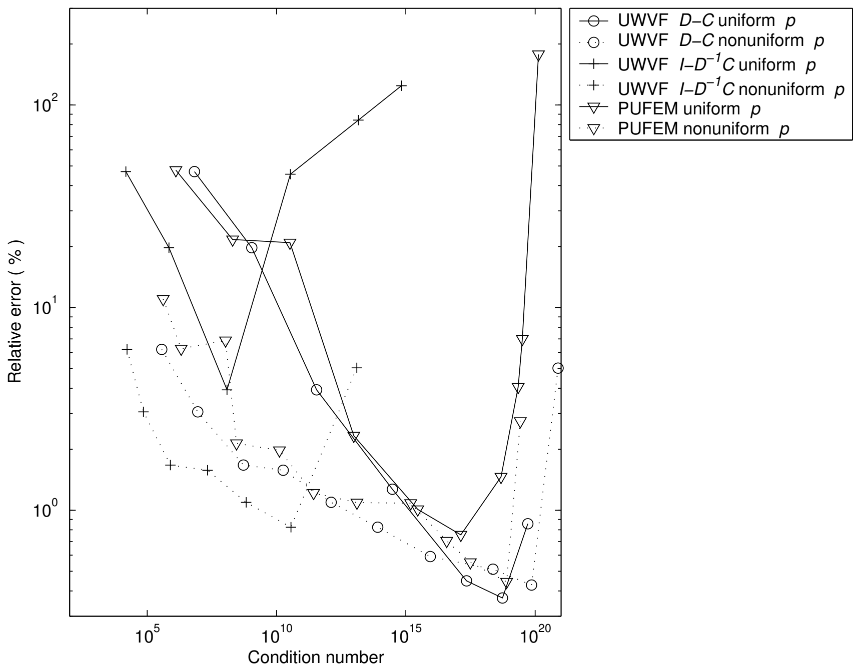

(b)

Fig. 5.9. Reproduced from [18]. A comparison of two approaches for choosing the number of plane wave basis functions. In the case of *uniform* enrichment, the basis dimension is the same throughout the whole computational domain Ω. The curves labeled with *non-uniform* enrichment are computed so that the basis dimension varies within the computational domain. The accuracy decreases by reaching a 'limit value' of the condition number

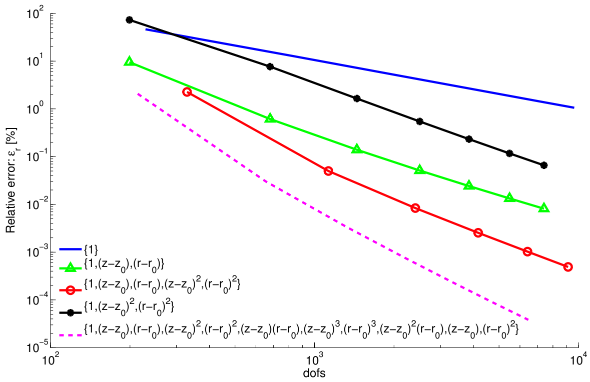

Fig. 5.10. Relative error [%] with respect to the number of degrees of freedom for the propagation at 800 Hz of the second radial mode of the first azimuthal order in a hard walled circular duct ($L = 2m; R_d = 0.5m$).

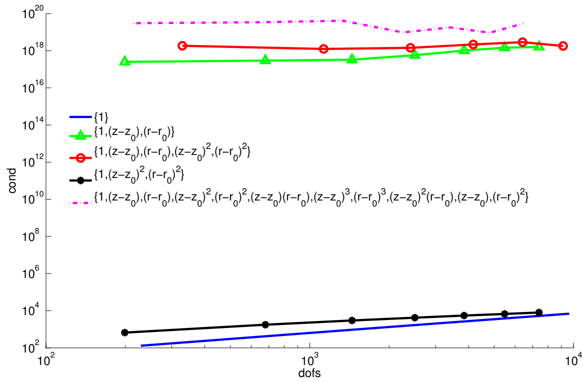

Fig. 5.11. Condition number with respect to the number of degrees of freedom for the propagation at 800 Hz of the second radial mode of the first azimuthal order in a hard walled circular duct ($L = 2m; R_d = 0.5m$).

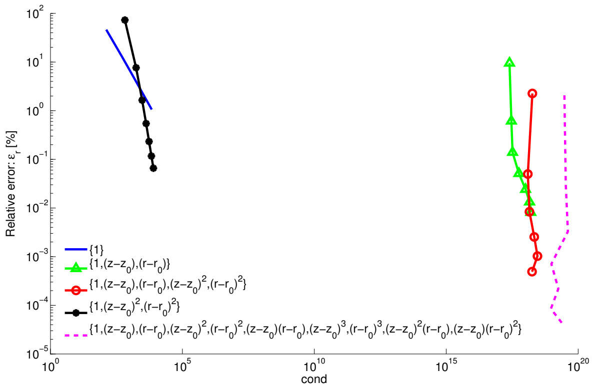

Fig. 5.12. Evolution of the relative error [%] with respect to the condition number for the propagation at 800 Hz of the second radial mode of the first azimuthal order in a hard walled circular duct ($L = 2m; R_d = 0.5m$).

5.2 Multipole radiation

We examine the parameters of the Mapped Infinite Partition of Unity Method and their effect on the accuracy. This takes into account the discretization (topology of elements, mapping), the radial and circumferential orders of the infinite elements, and the choice of the polynomial enrichment.

The performances of the Mapped Partition of Unity Infinite Element are analysed on two applications based on multipole radiation. The dipole ($N = 1$) and the multipole ($N = 7$) radiation.

5.2.1 Infinite element parameters

This section analyses the influence of the parameters of the infinite elements such as the radial m_0 or the circumferential b_0 order and the effect of the discretization (number and topology of infinite elements).

All the results from this section are computed for the multipole $N = 7$ radiation at 700Hz. The acceleration boundary condition is prescribed on the boundary $r_s = 1m$. The theory (section 2.8.1) recommends to use an infinite radial order of $m_0 = N + 1 = 8$.

We first examine the influence of the **radial order** of the infinite element. We decide to minimise the error due to other parameters such as the approximation in the inner region or the tangential approximation in the infinite elements. Hence, the interface Γ is taken close to the acceleration boundary condition $r_\Gamma = 1.01m$ and the inner mesh is generated with only one strip ($n_r = 1$) of mapped finite elements ($Q8$). The mesh size in the radial direction is equivalent to take 48 elements per wavelength ($\lambda = 0.485m$). In the circumferential direction the number of elements varies with the enrichment:

- $V_{ij} = \{1\}$ with $n_\theta = 280$,
- $V_{ij} = \left\{1, (z - z_0), (r - r_0), (z - z_0)^2, (r - r_0)^2\right\}$ with $n_\theta = 140$,
- $V_{ij} = \left\{1, (z - z_0), (r - r_0), (z - z_0)^2, (r - r_0)^2, (z - z_0)(r - r_0),\right.$
  $\left.(z - z_0)^3, (r - r_0)^3, (z - z_0)^2 (r - r_0), (z - z_0)(r - r_0)^2\right\}$ with $n_\theta = 100$

The number of elements in the circumferential direction is chosen to keep quite the same number of degrees of freedom whatever the enrichment (see table 5.3). The mesh (inner and outer regions) is very fine, we can then analyse the error due to the infinite radial approximation.

Figure 5.13 illustrates the evolution of the accuracy with the radial order m_0. The accuracy is represented by the L^2 relative error in the inner region. We expect the error to decrease with the radial order until the recommended value $m_0 = 8$ is reached. The decay

Degrees of freedom	$m_0 = 1$	$m_0 = 2$	$m_0 = 3$	$m_0 = 4$	$m_0 = 5$	$m_0 = 6$	$m_0 = 7$	$m_0 = 8$	$m_0 = 9$
V_{ij} constant - $b_0 = 1$	562	843	1124	1405	1686	1967	2248	2529	2810
V_{ij} quadratic - $b_0 = 1$	1410	1551	1692	1833	1974	2115	2256	2397	2538
V_{ij} quadratic - $b_0 = 2$	1410	1692	1974	2256	2538	2820	3102	3384	3666
V_{ij} cubic - $b_0 = 2$	2020	2222	2424	2626	2828	3030	3232	3434	3636

Table 5.3. Number of degrees of freedom for the different enrichments with respect to the infinite radial order.

of the error is the same for all the inner enrichments. This sounds logical as the mesh is very fine and the error is only due to the radial approximation in the infinite elements. As the radial functions are the same whatever the enrichment in the inner region or whatever the infinite circumferential functions, we observe that all curves are superimposed. Nevertheless, the behaviour becomes different as the infinite radial order gets close to $m_0 = 8$. We note that the error reaches a limit value. This is due to the accuracy of the approximation in the inner region and along the circumferential direction in the outer region. This error will drop if the mesh of the inner region is refined but is not dependent on the radial interpolation of the infinite elements. For instance, we observe that the use of a second infinite circumferential order $b_0 = 2$ with the quadratic enrichment is more accurate at high radial order than the case with $b_0 = 1$[3]. This verifies the fact that at a radial order close to $m_0 = 8$, the accuracy is led by the circumferential approximation.

The simulations are performed with a circumferential order equal to $b_0 = 1$ for the constant enrichment, $b_0 = \{1, 2\}$ for the quadratic enrichment and $b_0 = 2$ for the cubic enrichment. Other simulations show it is not interesting (from the accuracy point of view) to get higher infinite circumferential order than those used for this application.

The **infinite circumferential approximation** is analysed by varying the number of elements in the circumferential direction and comparing the simulations with different infinite circumferential orders ($b_0 = \{1, 2, 4\}$). The simulation of the multipole $N = 7$ radiation is performed by taking an inner region comprised between $r_S = 1m$ and $r_\Gamma = 3m$. The inner mesh is generated with $n_r = 100$ mapped Q8 elements in the radial direction and a variable number of elements in the circumferential one n_θ. The enrichment is composed of second order functions and the radial order of the infinite elements is $m_0 = 8$.

Whatever the circumferential order, the error decreases with the number of degrees of freedom (i.e.: n_θ) (fig. 5.14). We notice that the error is lower (nearly one order of magnitude) for the case $b_0 = 2$ than $b_0 = 1$ with coarse meshes. But this difference vanishes with fine meshes. This can be explained by the quality of the approximation in the infinite element. It exists two ways to improve the approximation: increasing the infinite polynomial order (increasing b_0) or increasing the number of elements. We notice

[3] This has also been observed by Astley [30] who noticed that quadratic infinite elements are more accurate than linear ones

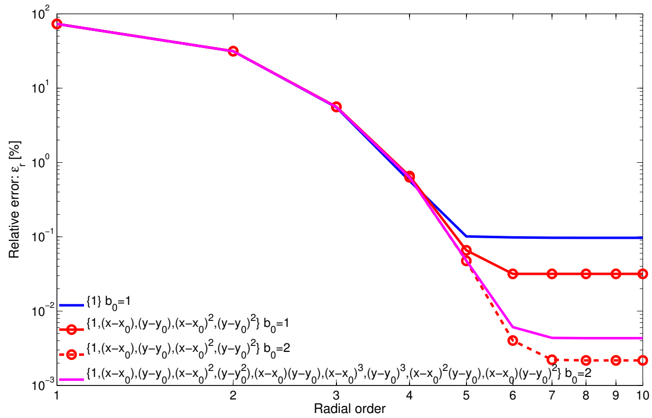

Fig. 5.13. Evolution of the accuracy with respect to the radial order of infinite functions for three different enrichments. The mesh is generated by one strip of elements between $r_S = 1m$ and $r_\Gamma = 1.01m$. Radiation of a multipole $N = 7$ at $700Hz\,(kr_S = 12.94)$.

an advantage to increase the polynomial enrichment rather than increasing the number of elements.

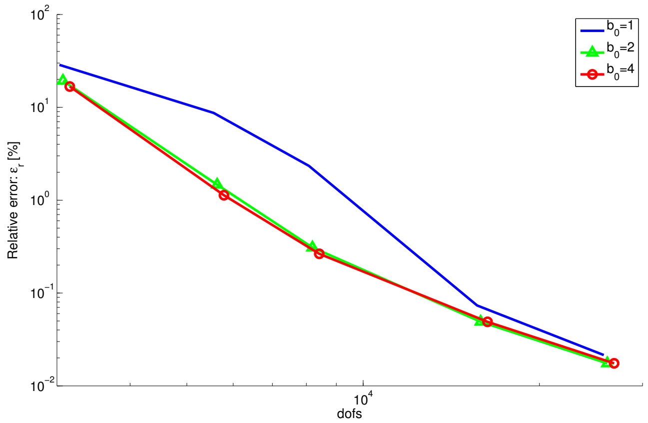

Fig. 5.14. Radiation of a multipole $N = 7$ at $700Hz\,(kr_S = 12.94)$, $r_S = 1m$, $r_\Gamma = 3m$, $n_r = 100$, second order enrichment. Influence of the number of elements in the circumferential direction (i.e. the number of infinite elements) and the the order of circumferential infinite function.

It is not necessary to increase the infinite circumferential order above $b_0 = 2$ (for this application). Figure 5.14 shows that the use of a circumferential order $b_0 = 4$ does not increase significantly the accuracy compared to the $b_0 = 2$ case. As the inner enrichment is of second order, these results show that it is not necessary to have a circumferential approximation of higher order in the outer region than in the inner one (as it does not improve the quality of the solution). The accuracy is dependent of the whole mesh and not only of the accuracy of the approximation in the outer region (infinite elements).

We also compare the choice of the enrichment in the inner region and the influence of the **type of the elements** (Q4 or Q8)[4]. We analyse the radiation of the multipole ($N = 7$) at 700 Hz. The inner region is defined by $r_S = 1m$ and $r_\Gamma = 1.01m$. It is meshed by one strip of elements $n_r = 1$. The infinite radial order is $m_0 = 7$ and the circumferential order $b_0 = 1$ for the constant enrichment $V_{jl} = 1$ and $b_0 = 2$ for the others (we verified that an increase of b_0 does not improve the accuracy measured by the L^2 relative error in the inner region).

Figure 5.15 illustrates the L^2 relative error in the inner region for the use of two different elements (Q4 and Q8) and two different numbers of elements in the circumferential direction ($n_\theta = 10\ or\ 30$). This shows that the use of Q8 elements has a huge impact on the quality of the solution. This can be explained by the improvement of the geometry and the improvement in the definition of the phase μ.

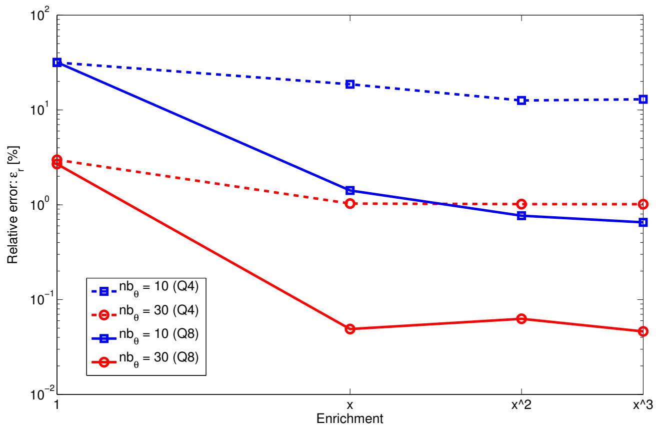

Fig. 5.15. Radiation of a multipole $N = 7$ at $700Hz\,(kr_S = 12.94)$, $r_S = 1m$, $r_\Gamma = 1.01m$, $n_r = 1$, nb_θ is the number of elements in the circumferential direction. Influence of the type of element on the accuracy.

The same analysis is performed by using the inner enrichment function as infinite circumferential functions. This is not detailed in the formulation chapter but it consists in using the same circumferential function for all the radial functions ($d = 1 : m_0$) instead of defining the $T_j^{d>1}$ (equation 2.152). The results are shown in figure 5.16. It compares the simulations where the circumferential functions are the same for all the radial functions with those where the circumferential functions for radial orders $d > 1$ are defined by the $T_j^{d>1}$ of equation 2.152. We notice that there is no improvement by using the same functions for the whole infinite radial orders. Moreover this formulation has some drawbacks such as the number of unknowns and the lack of robustness. If for instance we consider the

[4] Q4 are classic quadrangle elements with four nodes and linear edges. The related Q4 infinite elements have two nodes on the interface Γ and a linear edge. Q8 mapped elements are constructed with four nodes and four mapping points (described at section 2.9.1 and illustrated in figure 2.15). The related Q8 mapped infinite elements have two nodes on the interface Γ and one mapping point (described at section 2.9.3 and illustrated in figure 2.20). Note that the degrees of freedom are located at nodes but not on the mapping points

'cubic' enrichment (10 unknowns per node) in the inner region and an infinite radial order $m_0 = 7$, this means that each infinite node will have 70 unknowns. In the other case, the infinite circumferential order enrichment $b_0 = 2$ leads to 22 unknowns per infinite node (10 *for* $d = 1$ *and* 2 *for each* $d = 2:7$). The other drawback corresponds to cases where the infinite edge is along the r or the z direction. The enrichment function $(1 - r_0)^i$, for instance, is then equal to zero in the whole infinite element which creates zero lines and columns in the matrix. This leads to a singular problem.

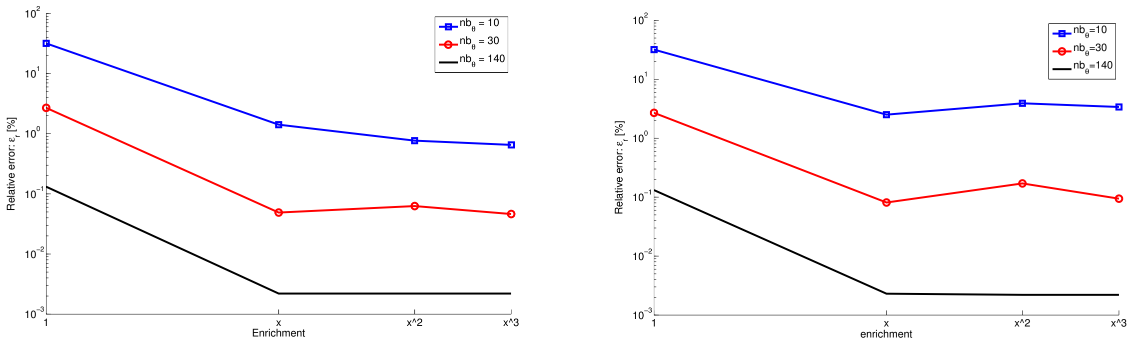

(a) (b)

Fig. 5.16. Influence of the discretization and the enrichment on the accuracy (a) Circumferential infinite functions are the same as the enrichment functions in the inner region (b) Use of circumferential functions given by equation 2.152. Multipole ($N = 7$) radiation: ($700Hz, kr_S = 12.94$), number of elements in the radial direction: $n_r = 1$, and in the circumferential one: $n_\theta = \{10, 30, 140\}$

We also obviously notice that if the infinite radial order is not appropriate ($m_0 = 3$), the error is bounded to the same value whatever the number elements in the circumferential direction (n_θ). This means that the error is due to the bad representation in the infinite direction radial direction and the accuracy does not improve by increasing the circumferential approximation.

From these analyses, we can conclude that the accuracy of a simulation in an infinite domain depends on several parameters. The radial order has to be appropriate: it depends on the complexity of the acoustic field within the infinite elements. The topology of the elements and the circumferential approximation has also a significant influence on the accuracy. We recommend here to use Q8 finite and infinite elements and circumferential infinite functions of order $b_0 = 2$ when the inner enrichment is higher than $V_{ij} = \{1\}$. A last obvious point to ensure good accuracy is to have a good approximation in the inner region as it has been observed in [30].

5.2.2 Dipole radiation: performance analysis

A convergence analysis is first performed on the dipole (figure 5.17) at 1100Hz. This figure gives the relative error with respect to the number of degrees of freedom. The meshes used for the computation contains the same number of elements along the radial direction as those along the circumferential one.

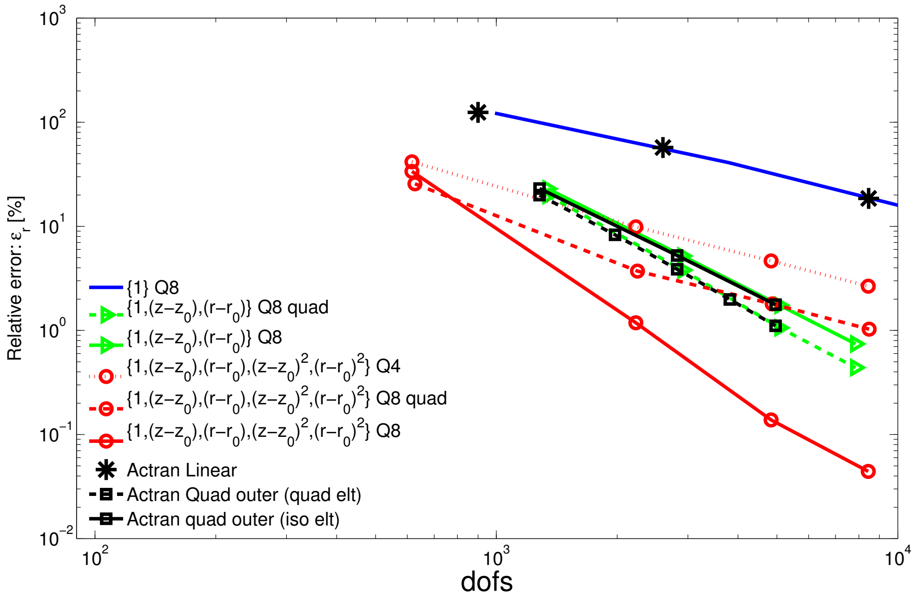

Fig. 5.17. Dipole radiation at 1100Hz ($kr_S = 20.3$): Convergence curves showing the relative error ε_r with respect to the number of degrees of freedom (dofs).

Several conclusions can be drawn from figure 5.17. It compares the proposed method with the Finite Element Method (linear and quadratic elements). It also shows the performances of the Mapped Infinite Elements developed.

The mesh used for Partition of Unity computations can be either Q4 elements or Q8 elements, whatever the enrichment. The Q4 element is a classical quadrangle element with four nodes and straight edges. Each node contains a number of degrees of freedom corresponding to the enrichment used. The Q8 element is described by four nodes at the corners of the element and four mapping points. These mapping points allow mapped elements with curved edges but they are not linked with degrees of freedom. The Q8 element possesses quadratic mapping functions but the Partition of Unity functions N_j remain bilinear functions.

Two different Q8 meshes are considered. The first one is an element mapped such as it matches as well as possible the geometry of the application. The second one is a Q8 element chosen such as it has the same topology than a Q4 element. This is the reason why it is called *Q8quad*, for quadrangle Q8 element.

The linear Finite Element Method and the ≪degenerated≫ Partition of Unity Method are similar and have the worst properties of all in terms of accuracy. Note that figure 5.17 shows the constant enrichment $\{1\}$, for the Q8 element only as other elements give results which superimposes the plotted Q8 curve. The quadratic Finite Element and the first order enrichment also correspond. The convergence rate for the second order enrichment with Q8 elements performs better than the others.

Looking at the second order enrichment (figure 5.17), the Q8 element is, as expected, more efficient than the Q4 one. The circular geometry is better represented with mapped elements. But one should expect the Q4 to have the same properties than the Q8*quad*, as they have the same geometry. It is not the case because the Q8 element, even with a quadrangle topology, improves the Infinite Element formulation, especially for the definition of the parameter μ (with the summation over two base nodes and one mapping point (Q8, Q8*quad*) instead of the summation over two base nodes ($Q4$)).

Figure 5.19 illustrates converged solutions bounded by an error of 5%. It represents the time required to solve the dipole radiation within the frequency range: 100Hz to 3600Hz. Figure 5.18 shows the coarsest mesh used for the simulation using the second order enrichment at 100 Hz. As for the previous case, the constant enrichment is only represented for the Q8 element. The two other types of elements (Q4, Q8 *quad*) give results close to the one on the figure. These curves confirms what was expected. The coupling of the method with infinite elements is effective and gives good results. This allows either for reducing the computational time while solving the same application or, for increasing the range of frequencies which can be analysed.

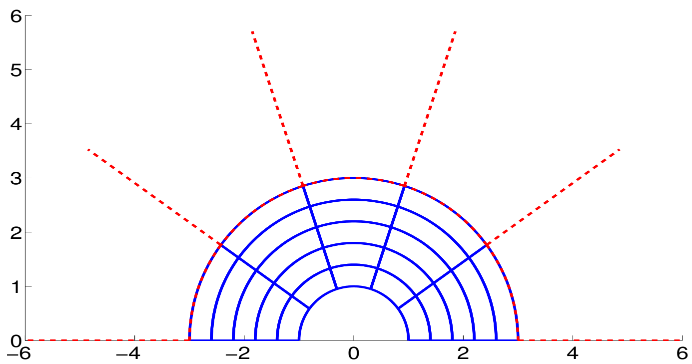

Fig. 5.18. Coarsest mesh used for the simulation of the dipole at 100 Hz with the second order enrichment. As it can be noticed, the inner region is partitioned with Q8 elements and dashed lines represent the infinite elements.

Note also that for each enrichment, the three discretizations tend to give the same results, except for the second order enrichment. In this case, there are 5 degrees of freedom per node. A small number of elements is thus sufficient to compute an accurate solution. However, this few number of elements does not allow a good representation of the circular geometry with Q4 elements. This is the reason why the Q8 element is more accurate than the Q4 one at small non-dimensional wavenumber.

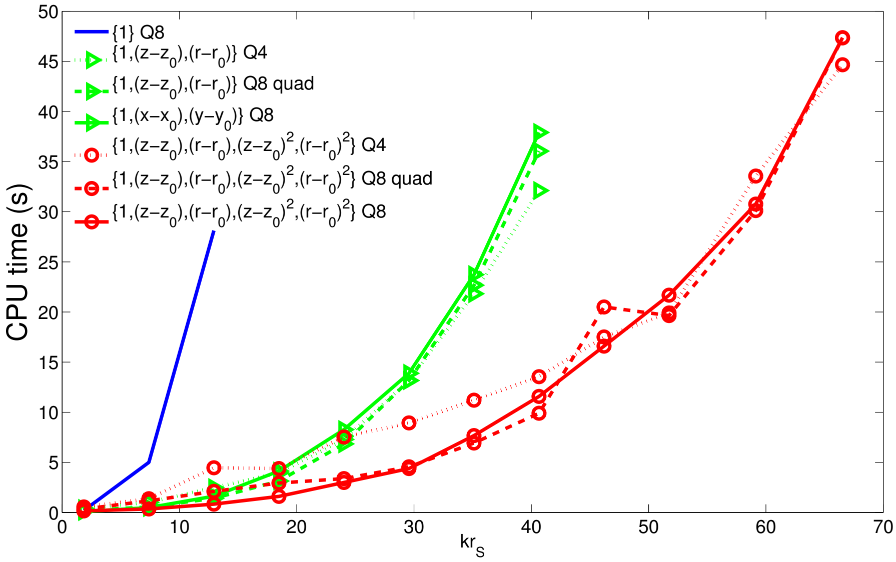

Fig. 5.19. Computational time (s) versus the non-dimensional wavenumber (kr_S) with an accuracy under 5%, frequency varying from 100Hz to 3600Hz.

We can draw the same conclusion as for the application without Infinite Elements. The Mapped Infinite Partition of Unity Method behaves like a p-FEM with infinite elements. The advantage of this method compared to a p-FEM is the ability to locally adapt the enrichment instead of refining mesh.

5.2.3 Multipole $N = 7$ radiation: performance analysis

The convergence curve analysing the accuracy of the numerical solution with respect of the number of degrees of freedom is shown in figure 5.20. It is obtained by the radiation of a multipole $N = 7$ at 700 Hz. The inner region is meshed with Q8 finite elements between $r_S = 1m$ and $r_\Gamma = 3m$. The number of elements varies and is proportional to $n_r = 5j$ and $n_\theta = 10j$. The infinite elements, attached to the interface Γ, are of infinite radial order $m_0 = 8$ and circumferential order: $b_0 = 1$ for $V_{jl} = \{1\}$ and $b_0 = 2$ for the others.

We illustrate the convergence rate of the enrichments. As expected the worst enrichment is the constant $V_{jl} = \{1\}$ which corresponds to the classic linear Finite Element Method. The convergence rate increases until enrichment order p=2. However, for enrichments equal or higher than p=4, the curves does not correspond to what was expected. The instabilities with high polynomial orders deteriorates the quality of the simulation.

Figure 5.21 illustrates the computational time required for the simulation with respect to the non dimensional wavenumber. We may also conclude that the most performant enrichment orders are p=2 or p=3. For higher orders, there is a 'loss' of performance.

We then recommend the use of polynomial enrichment of order 2 or 3 while the mesh is coupled to infinite elements.

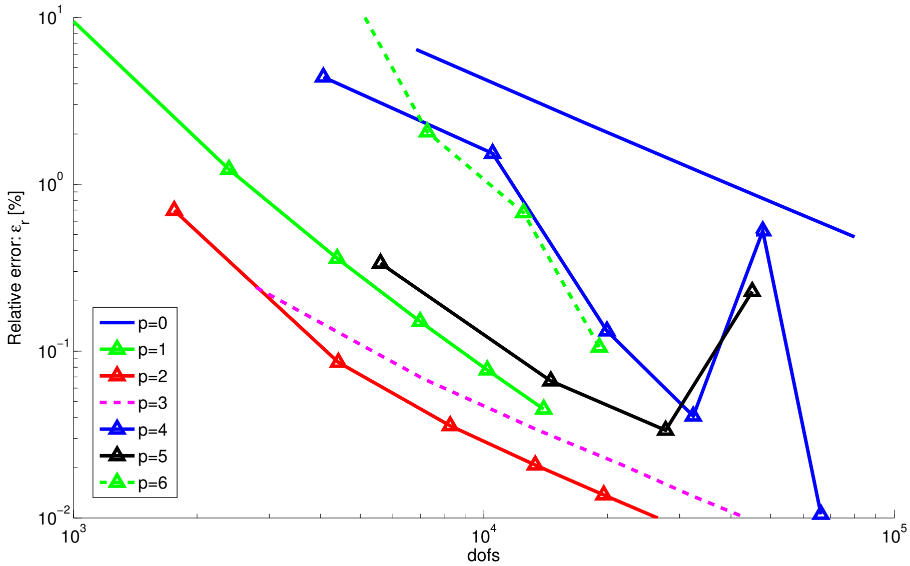

Fig. 5.20. Multipole ($N = 7$) radiation at 700Hz ($kr_S = 12.94$): Convergence curves showing the relative error ε_r with respect to the number of degrees of freedom (dofs).

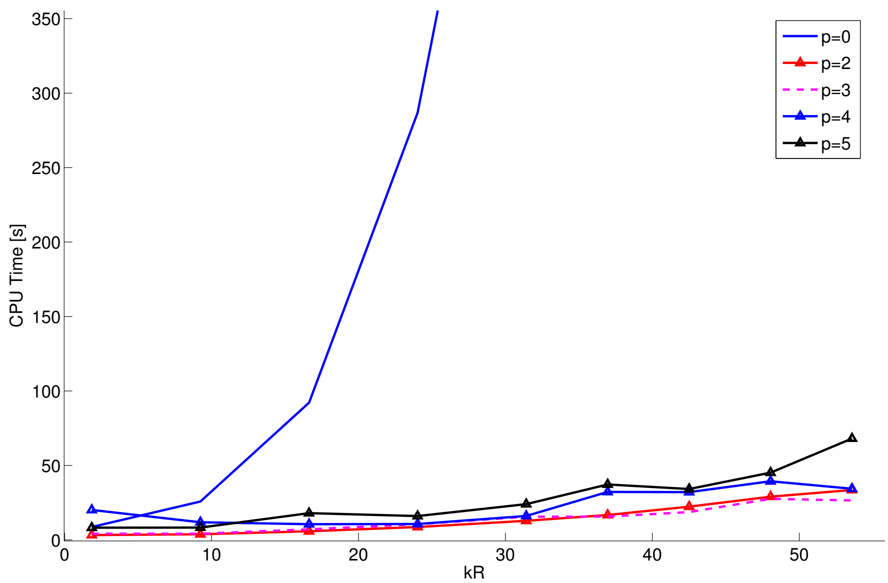

Fig. 5.21. Multipole ($N = 7$) radiation from 100Hz ($kr_S = 1.85$) to 2900Hz ($kr_S = 53.6$): Performance curves showing the required CPU time [s] with respect to the non dimensional wavenumber kR.

5.3 Rigid piston radiation

Convergence analyses have been performed to illustrate the performances. The convergence curves showing the L^2 relative error in the inner region with respect to the degrees of freedom compare the enrichment functions and the topology of the elements (Q4 or Q8). Two different interfaces have also been chosen (figures 5.22 and 5.24). The simulations have been performed with a frequency of 500 Hz and an infinite radial order $m_0 = 4$. The circumferential functions are of order $b_0 = 1$ for the constant enrichment and $b_0 = 2$ for the others (it has been verified that it is not necessary to increase further the circumferential approximation in the infinite elements).

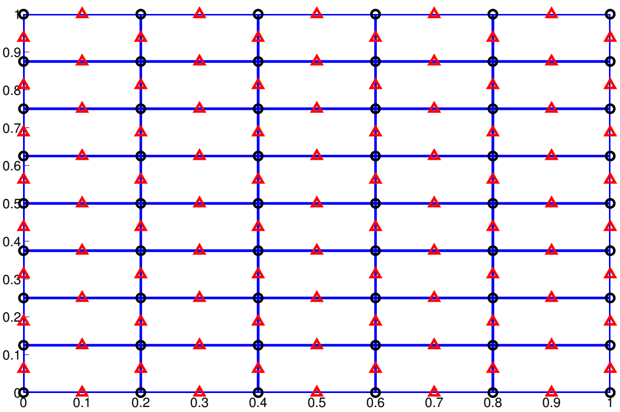

Fig. 5.22. Mesh of the inner region with the interface formed by two straight lines. The mesh is composed of 8 Q8 elements in the radial direction and 5 in the axial one. The nodes are represented by black circles and the mapping points by red triangles. The mesh with Q4 elements is the same as the one illustrated without the mapping points.

The results obtained for the first mesh (straight interface), are shown figure 5.23(b) for Q4 elements and figure 5.23(a) for mapped Q8 elements. The number of elements in the radial and in the axial directions are proportional to $2n$ and $n+1$, respectively. The results are similar for both types of elements except for the cubic enrichment. This means that at high polynomial order enrichments, the accuracy is dependent on the definition of the phase μ as it is the only difference between the two computations: same shape of elements, same number of degrees of freedom (the mapping points do not correspond to unknowns), same boundary conditions, same shape functions (inner enrichment, same radial and circumferential function).

The error stops decreasing after reaching a certain value. It has been found that this limitation is due to the accuracy of the analytical solution (equation 3.5) which has been evaluated by a numerical integration.

The same application has been analysed with an other interface Γ (figure 5.24). We take the same number of elements in the radial, in the axial directions and along the interface.

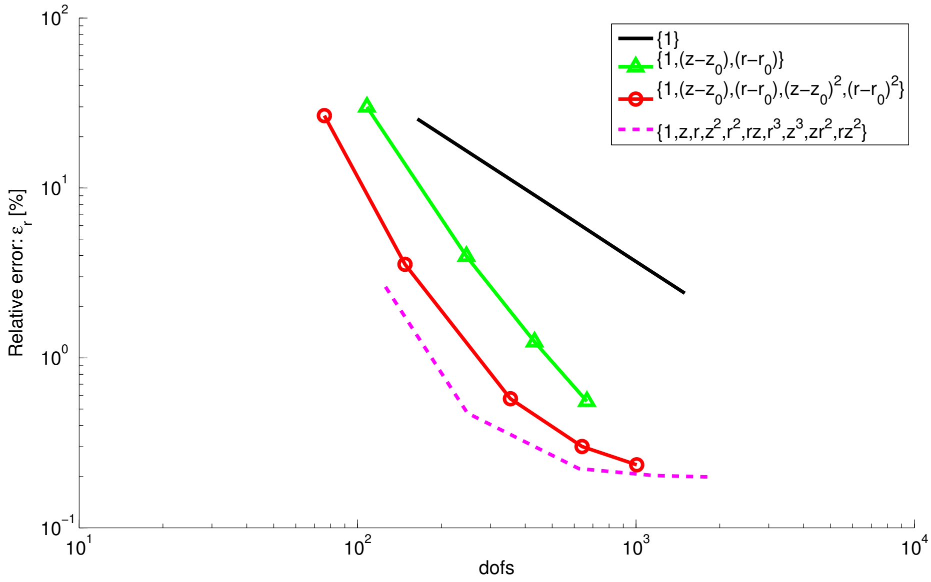

(a)

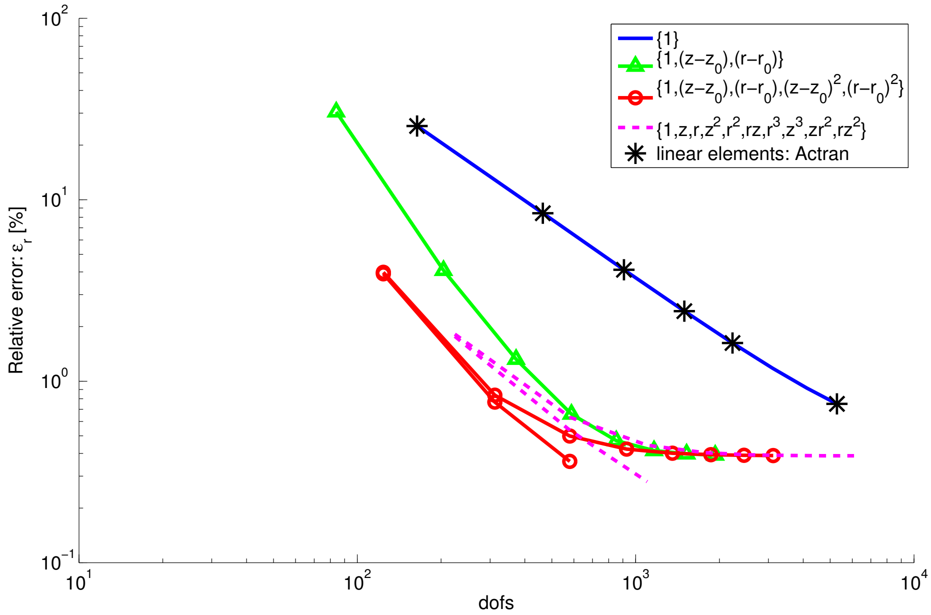

(b)

Fig. 5.23. Radiation of the piston at 500 Hz: Convergence curves showing the relative error ε_r with respect to the number of degrees of freedom (dofs) with the interface formed by two straight lines (a) mapped Q8 elements (b) Q4 elements. Two results exists for the second order and the cubic enrichment. The difference is the accuracy in the integration of the analytical solution, illustrating that the limitation of the error is due to the accuracy of the analytical solution. (Some simplifications have been made in the legend. For the cubic enrichment $\{z\}$, for instance, meant $\{z - z_0\}$).

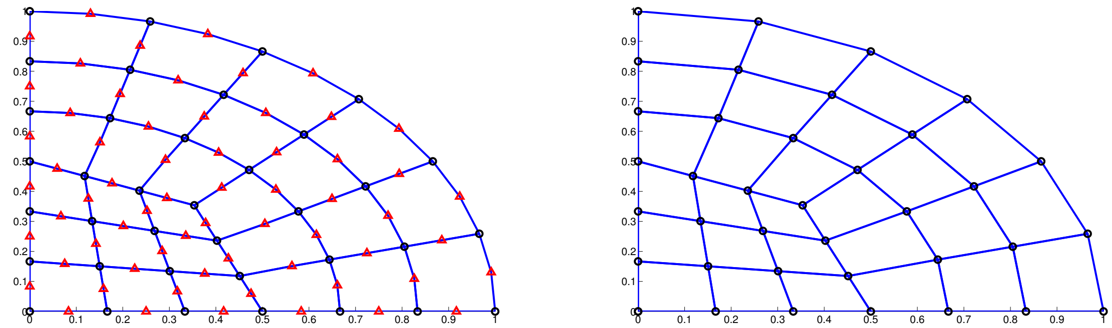

(a) (b)

Fig. 5.24. Mesh of the inner region with the interface formed by an open circle. The mesh is composed of 6 elements in the radial direction, 6 in the axial one and 6 along the interface Γ. The nodes are represented by black circles and the mapping points by red triangles. (a) mapped Q8 elements (b) Q4 elements.

The two topologies of elements are compared during a convergence analysis (figure 5.25). We clearly see that the mapped Q8 elements provide better accuracy than the Q4 one.

We then recommend the use of high order enrichment and mapped Q8 elements as the results obtained with Q4 and Q8 elements are quite the same or better for linear interfaces and more accurate for Q8 elements in the case of curved interfaces.

A performance analysis (figure 5.26) comparing the time required to compute a solution under an error of 5% with respect to a variation of the excitation frequency shows the advantage of using a high order enrichment instead of a constant enrichment.

We remark that the accuracy is not limited by the condition number. Even for very high condition number, we reach excellent accuracy: around 0.5% (fig. 5.27). For this application, the error is bounded by the quality of the analytical solution (obtained by numerical integration).

5.4 Conclusion

This chapter analyses the characteristics of the axisymmetric Mapped Infinite Partition of Unity Method.

Convergence and performance analyses explore the accuracy and the efficiency of the method for cavities and exterior applications. This leads us to suggest high order enrichment for Mapped Infinite Partition of Unity simulations.

A section on the conditioning shows that the method leads to high condition numbers. This has no influence on the solution as we use an appropriate solver. Bad conditioning does not prevent for convergence but may perturb the accuracy. Then we recommend the use of preconditioning.

We also showed that the method could be used to improve locally the approximation. This can been done by enriching the nodes where the approximation has to be modified. We showed that this technique prevent for remeshing and leads to improved accuracy in the whole domain.

The sections on exterior applications analysed the effect of radial and circumferential infinite functions. They also illustrated the interest of meshing the domain with mapped $Q8$ elements instead of the classical $Q4$ ones.

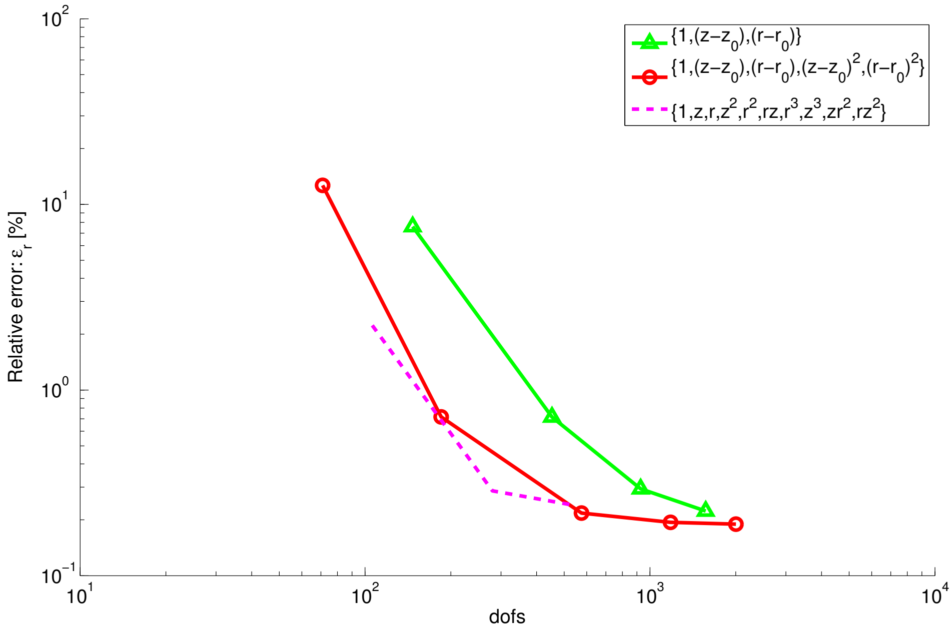

(a)

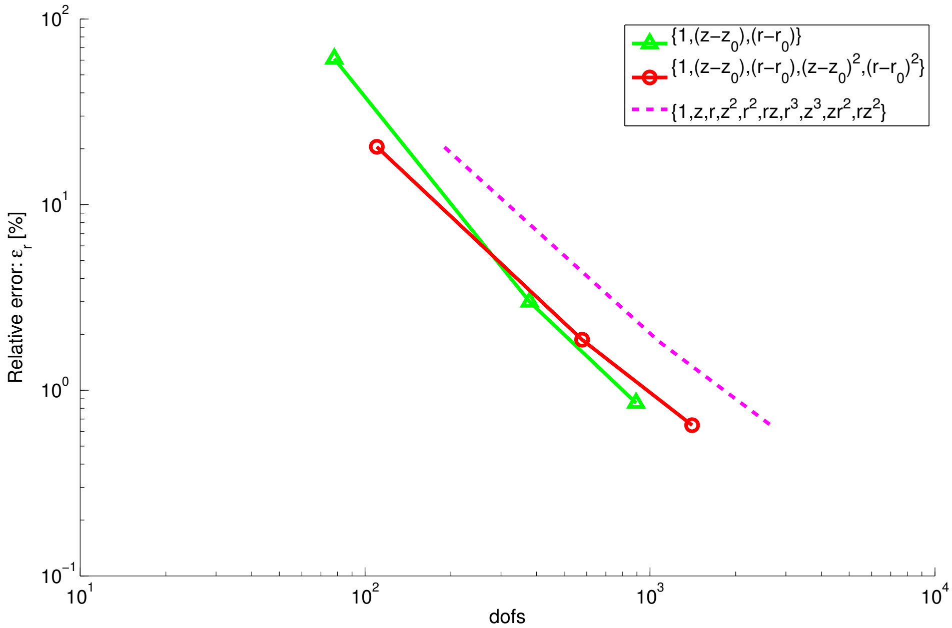

(b)

Fig. 5.25. Radiation of the piston at 500 Hz: Convergence curves showing the relative error ε_r with respect to the number of degrees of freedom (dofs) with the interface formed by an open circle (a) mapped Q8 elements (b) Q4 elements. (Some simplifications have been made in the legend. For the cubic enrichment $\{z\}$, for instance, meant $\{z - z_0\}$).

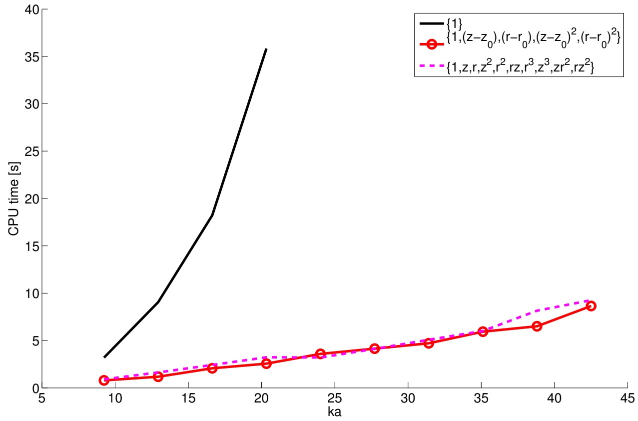

Fig. 5.26. Radiation of the piston at 500 Hz: Curves showing the computational time (s) versus the non-dimensional wavenumber (kr_p) with an accuracy under 5% with the interface formed by two straight lines for Q8 elements . (Some simplifications have been made in the legend. For the cubic enrichment $\{z\}$, for instance, meant $\{z - z_0\}$).

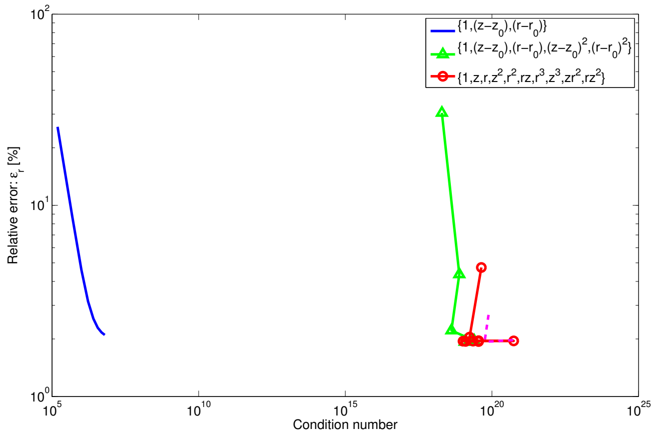

Fig. 5.27. Radiation of the piston at 500 Hz: Curves showing the relative error ε_r with respect to the condition number with the interface formed by two straight lines for Q4 elements. (Some simplifications have been made in the legend. For the cubic enrichment $\{z\}$, for instance, meant $\{z - z_0\}$).

References

1. Ph. Bouillard, F. Ihlenburg, Error estimation and adaptivity for the finite element solution in acoustics: 2D and 3D applications, Comput. Methods Appl. Mech. Engrg. 176 (1999) 147-163.
2. F. Ihlenburg, I. Babuška, Dispersion analysis and error estimation of Galerkin finite element methods for the Helmholtz equation, Int. J. Numer. Methods Eng. 38 (1995) 3745-3774.
3. J.T. Oden, S. Prudhomme, L. Demkowicz, A posteriori error estimation for acoustic wave propagation problems, Arch. Comput. Meth. Engng. 12 (2005) 343-389.
4. F. Ihlenburg, I. Babuška, Finite element solution of the Helmholtz equation with high wave number part II : the h-p version of the FEM, SIAM J. Numer. Anal. 34 (1997) 315-358.
5. O.C. Zienkiewicz, Achievements and some unsolved problems of the finite element method, Int. J. Numer. Methods Eng. 47 (2000) 9-28.
6. L.L. Thompson, A review of finite element methods for time-harmonic acoustics, J. Acoust. Soc. Am. 119 (2006) 1315-1330.
7. J.M. Melenk, I. Babuška, The partition of unity finite element method: basic theory and applications, Comput. Methods Appl. Mech. Engrg. 139 (1996) 289-314.
8. I. Babuška, J.M. Melenk, The Partition of Unity Method, Int. J. Numer. Methods Eng. 40 (1997) 727-758.
9. O. Laghrouche, P. Bettess, R. J. Astley, Modeling of short wave diffraction problems using approximating systems of plane waves, Int. J. Numer. Methods Eng. 54 (2002) 1501-1533.
10. Th. Strouboulis, I. Babuška, R. Hidajat, The generalized finite element method for Helmholtz equation: Theory, computation, and open problems, Comput. Methods Appl. Mech. Engrg. 195 (2006) 4711-4731.
11. Th. Strouboulis, R. Hidajat, I. Babuška, The generalized finite element method for Helmholtz equation Part II: Effect of choice of handbook functions, error due to absorbing boundary conditions and its assessment, Comput. Methods Appl. Mech. Engrg. 197 (2008) 364-380.
12. Th. Strouboulis, K. Copps, I. Babuška, The generalized finite element method, Comput. Methods Appl. Mech. Engrg. 190 (2001) 4081-4193.
13. Th. Strouboulis, I. Babuška, K. Copps, The design and analysis of the generalized finite element method, Comput. Methods Appl. Mech. Engrg. 181 (2000) 43-69.
14. C. Farhat, I. Harari, L.P. Franca, The discontinuous enrichment method, Comput. Methods Appl. Mech. Engrg. 190 (2001) 6455-6479.
15. B. Pluymers, W. Desmet, D. Vandepitte, P. Sas, Application of an efficient wave-based prediction technique for the analysis of vibro-acoustic radiation problems, J. Comput. Appl. Math. 168 (2004) 353-364.
16. P. Gamallo, R.J. Astley, A comparison of two Trefftz-type methods: The ultraweak variational formulation and the least-squares method, for solving shortwave 2-D Helmholtz problems, Int. J. Numer. Methods Eng. 71 (2007) 406-432.
17. P. Gamallo, R.J. Astley, The partition of unity finite element method for short wave acoustic propagation on non-uniform potential flows, Int. J. Numer. Methods Eng. 65 (2006) 425-444.
18. T. Huttunen, P. Gamallo, R.J. Astley, Comparison of two wave element methods for the Helmholtz problem, Commun. Numer. Meth. Engng. Article in Press (2008) doi:10.1002/cnm1102.
19. T. Huttunen, P. Monk, J.P. Kaipio, Computational aspects of the ultra weak variational formulation, J. Comput. Phys. 182 (2002) 27-46.
20. T. Huttunen, J.P. Kaipio, P. Monk, An ultra weak method for acoustic fluid-solid interaction, J. Comput. Appl Math. 213 (2008) 166-185.

21. P. Monk, D.-Q. Wang, A least squares method for the Helmholtz equation, Comput. Methods Appl. Mech. Engrg. 175 (1999) 121-136.
22. R. Sevilla, S. Fernández-Méndez, A. Huerta, NURBS-enhanced finite element method (NEFEM), Int. J. Numer. Methods Eng. Early ViewW (2008) doi: 10.1002/nme.2311
23. E. Chadwick, P. Bettess, O. Laghrouche, Diffraction of short waves modeled using new mapped wave envelope finite and infinite elements, Int. J. Numer. Methods Eng. 45 (1999) 335-354.
24. E. De Bel, P. Villon, Ph. Bouillard, Forced vibrations in the medium frequency range solved by a partition of unity method with local information, Int. J. Numer. Methods Eng. 162 (2004) 1105-1126.
25. L. Hazard, Ph. Bouillard, Structural dynamics of viscoelastic sandwich plates by the partition of unity finite element method, Comput. Methods Appl. Mech. Engrg. 196 (2007) 4101-4116.
26. T.J.R. Hughes, J.A. Cotrell, Y. Bazilevs, Isogeometric analysis: CAD, finite elements, NURBS, exact geometry and mesh refinement, Comput. Methods Appl. Mech. Engrg. 194 (2005) 4135-4195.
27. B. Szabó, A. Düster, E. Rank, The p-version of the finite element method, in: E. Stein, R. de Borst, T.J.R. Hughes (Eds.), Fundamentals, Encyclopedia of Computational Mechanics, vol. 1, Wiley, New York, 2004 (Chapter 5).
28. R.J. Astley, P. Gamallo, Special short wave elements for flow acoustics, Comput. Methods Appl. Mech. Engrg. 194 (2005) 341-353.
29. R.J. Astley, P. Gamallo, The Partition of Unity Finite Element Method for Short Wave Acoustic Propagation on Non-uniform Potential Flows, Int. J. Numer. Methods Eng. 65 (2006) 425-444.
30. R.J. Astley, G.J. Macaulay, J.-P. Coyette, L. Cremers, Three-dimensional wave-envelope elements of variable order for acoustic radiation and scattering. Part I. Formulation in the frequency domain, J. Acoust. Soc. Am. 103 (1998) 49-63.
31. R.J. Astley, J.-P. Coyette, Conditioning of infinite element schemes for wave problems, Commun. Numer. Meth. Engng. 17 (2001) 31-41.
32. D. Dreyer, O. von Estorff, Improved conditioning of infinite elements for exterior acoustics, Int. J. Numer. Methods Eng. 58 (2003) 933-953.
33. J.J. Shirron, I. Babuška, A comparison of approximate boundary conditions and infinite element methods for exterior Helmholtz problems, Comput. Methods Appl. Mech. Engrg. 164 (1998) 121-139
34. D. Dreyer, Efficient infinite elements for exterior acoustics, PhD thesis, Shaker Verlag, Aachen, 2004.
35. W. Eversman, Mapped infinite wave envelope elements for acoustic radiation in a uniformly moving medium, J. Sound Vib. 224 (1999) 665-687.
36. S.J. Rienstra, W. Eversman, A numerical comparison between the multiple-scales and finite-element solution for sound propagation in lined flow ducts, J. Fluid Mech. 437 (2001) 367-384.
37. S.J. Rienstra, Sound transmission in slowly varying circular and annular lined ducts with flow, J. Fluid Mech. 380 (1999) 279-296.
38. S.J. Rienstra, The Webster equation revisited, 8th AIAA/CEAS Aeroacoustic conference (2002) AIAA 2002-2520.
39. M.K. Myers, On the acoustic boundary condition in the presence of flow, J. Sound Vib. 71 (1980) 429-434.
40. T. Mertens, Meshless modeling of acoustic radiation in infinite domains, Travail de spécialisation, Université Libre de Bruxelles (U.L.B.), 2005.
41. W. Eversman, The boundary condition at an impedance wall in a non-uniform duct with potential mean flow, J. Sound Vib. 246 (2001) 63-69.
42. B. Regan, J. Eaton, Modeling the influence of acoustic liner non-uniformities on duct modes, J. Sound Vib. 219 (1999) 859-879.
43. H.-S. Oh, J.G. Kim, W.-T. Hong, The Piecewise Polynomial Partition of Unity Functions for the Generalized Finite Element Methods, Comput. Methods Appl. Mech. Engrg. Accepted manuscript (2008), doi: 10.1016/j.cma.2008.02.035.
44. Free Field Technologies, Actran user's manual, http://fft.be.
45. University of Florida, Department of Computer and Information Science and Engineering, http://www.cise.ufl.edu/research/sparse/umfpack/
46. T.A. Davis, A column pre-ordering strategy for the unsymmetric-pattern multifrontal method, ACM Transactions on Mathematical Software 30 (2004) 165-195.
47. T.A. Davis, Algorithm 832: UMFPACK, an unsymmetric-pattern multifrontal method, ACM Transactions on Mathematical Software 30 (2004) 196-199.
48. T.A. Davis and I.S. Duff, A combined unifrontal/multifrontal method for unsymmetric sparse matrices, ACM Transactions on Mathematical Software 25 (1999) 1-19.

49. T.A. Davis and I.S. Duff, An unsymmetric-pattern multifrontal method for sparse LU factorization, SIAM Journal on Matrix Analysis and Applications 18 (1997) 140-158.
50. A. Hirschberg, S.W. Rienstra, An introduction to aeroacoustics, Eindhoven University of Technology (2004).
51. G. Warzée, Mécanique des solides et des fluides, Université Libre de Bruxelles (2005).
52. M.J. Crocker, Handbook of acoustics, Wiley-Interscience, New York (1998).
53. R. Sugimoto, P. Bettess, J. Trevelyan, A numerical integration scheme for special quadrilateral finite elements for the helmholtz equation, Commun. Numer. Meth. Engng. 19 (2003) 233-245.
54. G. Gabard, R.J. Astley, A computational mode-matching approach for sound propagation in three-dimensional ducts with flow, J. Sound Vib. Article in Press (2008) doi:10.1016/j.jsv.2008.02.015.
55. C. Farhat, I. Harari, U. Hetmaniuk, A discontinuous Galerkin method with Lagrange multipliers for the solution of Helmholtz problems in the mid-frequency regime, Comput. Methods Appl. Mech. Engrg. 192 (2003) 1389-1419.
56. C.L. Morfey, Acoustic energy in non-uniform flows, J. Sound Vib. 14 (1971) 159-170.
57. F. Magoules, I. Harari (editors), Special issue on Absorbing Boundary Conditions, Comput. Methods Appl. Mech. Engrg. 195 (2006) 3354-3902.
58. M. Fischer, U. Gauger, L. Gaul, A multipole Galerkin boundary element method for acoustics, Engineering Analysis with Boundary Elements 28 (2004) 155-162.
59. J.-P. Bérenger, Three-dimensional Perfectly Matched Layer for the absorption of electromagnetic waves, J. Comput. Phys. 127 (1996) 363-379.
60. C. Michler, L. Demkowicz, J. Kurtz, D. Pardo, Improving the performance of Perfectly Matched Layers by means of hp-adaptivity, Numerical Methods for Partial Differential Equations 23 (2007) 832-858.
61. A. Bayliss, E. Turkel, Radiation boundary conditions for wave-like equations, Comm. Pure Appl. Math. 33 (1980) 707-725.
62. B. Engquist, A. Majda, Radiation boundary conditions for acoustic and elastic wave calculations, Comm. Pure Appl. Math. 32 (1979) 313-357.
63. K. Feng, Finite element method and natural boundary reduction, Proceedings of the International Congress of Mathematicians, Warsaw (1983) 1439-1453.
64. D. Givoli, B. Neta, High-order non-reflecting boundary scheme for time-dependent waves, J. Comput. Phys. 186 (2003) 24-46.
65. T. Hagstrom, A. Mar-Or, D. Givoli, High-order local absorbing conditions for the wave equation: Extensions and improvements, J. Comput. Phys. 227 (2008) 3322-3357.
66. T. Hagstrom, T. Warburton, A new auxiliary variable formulation of high-order local radiation boundary conditions: corner compatibility conditions and extensions to first order systems, Wave Motion 39 (2004) 327-338.
67. A. Hirschberg, S.W. Rienstra, An introduction to aeroacoustics, Eindhoven university of technology (2004).
68. V. Lacroix, Ph. Bouillard, P. Villon, An iterative defect-correction type meshless method for acoustics, Int. J. Numer. Meth. Engng 57 (2003) 2131-2146.
69. T. Mertens, P. Gamallo, R. J. Astley, Ph. Bouillard, A mapped finite and infinite partition of unity method for convected acoustic radiation in axisymmetric domains, Comput. Methods Appl. Mech. Engrg. 197 (2008) 4273-4283.
70. G. Gabard, Discontinuous Galerkin methods with plane waves for time harmonic problems, J. Comput. Phys. 225 (2007) 1961-1984.
71. L. Hazard, Design of viscoelastic damping for vibration and noise control: modeling, experiments and optimisation, PhD thesis, Univesité Libre de Bruxelles (2007).
72. G. Gabard, R.J. Astley, M. Ben Tahar, Stability and accuracy of finite element methods for flow acoustics. I: general theory and application to one-dimensional propagation, Int. J. Numer. Meth. Eng. 63, (2005) 947-973.
73. G. Gabard, R.J. Astley, M. Ben Tahar, Stability and accuracy of finite element methods for flow acoustics. II: Two-dimensional effects, Int. J. Numer. Meth. Eng. 63 (2005) 974-987.
74. A. Goldstein, Steady state unfocused circular aperture beam patterns in non attenuating and attenuating fluids, J. Acoust. Soc. Am. 115 (2004) 99-110.
75. T. Douglas Mast, F. Yu, Simplified expansions for radiation from baffled circular piston, J. Acoust. Soc. Am. 118 (2005) 3457-3464.
76. T. Hasegawa, N. Inoue, K Matsuzawa, A new rigorous expansion for the velocity potential of a circular piston source, J. Acoust. Soc. Am. 74 (1983) 1044-1047.
77. R.J. Astley, A finite element, wave envelope formulation for acoustical radiation in moving flows, J. Sound Vib. 103 (1985) 471-485.
78. J.M. Tyler, T.G. Sofrin, Axial flow compressor noise studies, SAE Transactions 70 (1962) 309-332.

79. M.C. Duta, M.B. Giles, A three-dimensional hybrid finite element/spectral analysis of noise radiation from turbofan inlets, J. Sound Vib. 296 (2006) 623-642.
80. H.H. Brouwer, S.W. Rienstra, Aeroacoustics research in Europe: The CEAS-ASC report on 2007 highlights, J. Sound Vib. Article in Press (2008) doi:10.1016/j.jsv.2008.07.020.
81. http://en.wikipedia.org/wiki/Aircraft_noise, 4th September 2008.
82. Y. Park, S. Kim, S. Lee, C. Cheong, Numerical investigation on radiation characteristics of discrete-frequency noise from scarf and scoop aero-intakes, Appl. Acoust. Article in press (2008) doi:10.1016/j.apacoust.2007.09.005.
83. General Electric Company, http://www.ge.com, http://www.turbokart.com/about_ge90.htm, 4th September 2008.
84. R.J. Astley, J.A. Hamilton, Modeling tone propagation from turbofan inlets - The effect of extended lip liner, AIAA paper 2002-2449 (2002).
85. V. Decouvreur, Updating acoustic models: a constitutive relation error approach, PhD thesis, Université Libre de Bruxelles (2008).
86. P.A. Nelson, O. Kirkeby, T. Takeuchi, and H. Hamada, Sound fields for the production of virtual acoustic images, Letters to the editor, J. Sound Vib. 204 (1999) 386-396.
87. Y. Reymen, W. De Roeck , G. Rubio, M. Bealmans, W. Desmet, A 3D Discontinuous Galerkin Method for aeroacoustic propagation, Proceedings of the 12th International Congress on Sound and Vibration 2005.
88. G. Gabard, Exact integration of polynomial-exponential products with an application to wave based numerical methods, Commun. Numer. Meth. Engng (2008) doi: 10.1002/cnm.1123.
89. New York University, http://math.nyu.edu/faculty/greengar/shortcourse_fmm.pdf, 1st december 2008.